

AD-A235 031



## ITION PAGE

Form Approved  
GSA No. 0704-0108

1. AGENCY USE ONLY (Leave Blank)			2. REPORT DATE 1991 March 22	3. REPORT TYPE AND DATES COVERED Annual 03/90 - 02/91
4. TITLE AND SUBTITLE  Pressureless Densification of Ceramic Matrix Composites			5. FUNDING NUMBERS AFOSR 2306-0267	
6. AUTHOR(S)  M. N. Rahaman, L. R. Dharani, R. E. Moore				
7. PERFORMING ORGANIZATION NAME(S) AND ADDRESS(ES)  The University of Missouri-Rolla Rolla, MO 65401			8. PERFORMING ORGANIZATION REPORT NUMBER AFOSR-TP-11313	
9. SPONSORING/MONITORING AGENCY NAME(S) AND ADDRESS(ES)  Dr. Liselotte J. Schioler Air Force Office of Scientific Research/NE Bolling Air Force Base Washington, DC 20332			10. SPONSORING/MONITORING AGENCY REPORT NUMBER 2306/A2	
11. SUPPLEMENTARY NOTES				
12a. DISTRIBUTION/AVAILABILITY STATEMENT  unlimited			12b. DISTRIBUTION CODE APR 20 1991	
13. ABSTRACT (Maximum 200 words)  In the first reporting period, experimental and theoretical studies were performed to determine the effect of key material and processing parameters on the sintering of model ceramic composites.  Experimentally, the effect of coarse inclusions ( $ZrO_2$ ) on the sintering of a fine-grained matrix ( $ZnO$ ) was highly dependent on the forming method. Kinetic data and microstructural observations indicated that the main factors controlling sintering were the packing of the matrix immediately surrounding the inclusions and interactions between the inclusions. A forming method for alleviating these two problems was investigated. Using this method, composites with up to 35 v% inclusions were sintered to full density under identical conditions used for the pure matrix.  Theoretically, a finite element program was developed to describe the kinetic data over the entire sintering process. Transient stresses were calculated incrementally from the density-time data and used to predict the reduction in the sintering rate. The effects of single and multiple inclusions and heterogeneity in the matrix density were calculated.				
14. SUBJECT TERMS  Ceramic matrix composites, sintering, theoretical modelling.			15. NUMBER OF PAGES 82	16. PRICE CODE
17. SECURITY CLASSIFICATION OF REPORT Unclassified	18. SECURITY CLASSIFICATION OF THIS PAGE Unclassified	19. SECURITY CLASSIFICATION OF ABSTRACT Unclassified	20. LIMITATION OF ABSTRACT UL	

# PRESSURELESS DENSIFICATION OF CERAMIC MATRIX COMPOSITES

## CONTENTS

	Page
Cover Page	
1. Statement of Work .....	2
2. Status of the Research .....	3
2.1 Introduction .....	3
2.2 Experimental Investigations .....	6
2.3 Theoretical Modelling.....	44
2.4 Summary of Accomplishments .....	67
2.5 Future Work.....	69
2.6 References .....	70
3. Publications .....	74
4. Professional Personnel .....	75
5. Interactions .....	75
Appendix.....	A1

RECEIPTED  
JULY 26 1988

Accession For	
NTIS NUMBER	<input checked="" type="checkbox"/>
DTIC NUMBER	<input type="checkbox"/>
Original used	<input type="checkbox"/>
Justification	
By _____	
Distribution	
Availability Codes	
Avail And/or Request	Special
A-1	

## **1. STATEMENT OF WORK**

Earlier work has shown that the presence of dense second phase inclusions typical for particulate or whisker reinforced systems can cause substantially reduced densification rates in a polycrystalline powder matrix. While a number of explanations have been put forward to explain the reduced sinterability, the mechanism is still ambiguous.

The objective of the research effort is to determine the factors that control the conventional pressureless sintering of polycrystalline ceramic matrix composites.

The approach is:

- (i) investigate how the sintering of model composites is controlled by key material and processing parameters (including the volume fraction, size and distribution of the reinforcement phase, the uniformity of the matrix, and the sintering temperature), and
- (ii) model the observed behavior.

## **2. STATUS OF RESEARCH**

### **2.1 INTRODUCTION**

This annual technical report provides a description of the work completed in the first year of a three-year program whose aim is to provide a basic understanding of the processes that control the sintering of polycrystalline ceramic matrix composites so that materials with high density and controlled microstructure can be processed successfully by conventional sintering.

Experimental studies<sup>1-3</sup> have shown that densification rate of a polycrystalline powder matrix is significantly reduced, even at modest volume fractions of a dispersed particulate reinforcement phase. The reduction in the densification rate of glass matrices is much smaller for an equivalent inclusion content<sup>4</sup>. While a number of explanations<sup>5-15</sup> have been put forward, the mechanism for the reduced sinterability of polycrystalline matrix composites is still ambiguous.

Experimental and theoretical studies were carried out to investigate how the sintering of model composites is controlled by key material and processing parameters (e.g. inclusion volume fraction, inclusion size, inclusion distribution, matrix uniformity and sintering temperature). The studies were initiated for a polycrystalline composite system consisting of a fine-grained matrix ( $ZnO$ ) and an inert, rigid, particulate inclusion phase ( $ZrO_2$ ).  $ZnO$  was used as the matrix phase for these initial studies because it can be sintered to full density within the temperature range of an existing dilatometer (1600 °C).

To provide further insight into the processes influencing sintering, green composite bodies were formed by three different processing techniques: (a) conventional mixing of the matrix and inclusion powders followed by die-pressing (hereafter called "conventional

processing"), (b) slip casting, and (c) coating the inclusion particles with the matrix powder by in-situ chemical precipitation followed by die-pressing (referred to as "coated particles"). For the present report, it is convenient to describe the experiments for the three processing techniques separately (Sections 2.2.1 - 2.2.3).

An important issue is the effect of the inclusion phase on the viscosity of the composite. The dependence of the composite viscosity on the volume fraction and size of the inclusion phase can provide insight into the importance of inclusion-inclusion and inclusion-matrix interactions and how they affect sintering. It is also important to determine whether the effect of an inclusion phase on the viscosity of a glass matrix is qualitatively different from that for a polycrystalline matrix. The effect of spherical nickel particles on the viscosity of a soda-lime glass matrix composite has been measured. Glass was chosen as the matrix phase for the initial phase of this study to eliminate the complexities of grain growth. Current work is examining the effect of  $ZrO_2$  inclusions on the viscosity of a  $ZnO$  matrix composite. The effect of the inclusions on the viscosity of the glass matrix composite forms the fourth part of the experimental research (Section 2.2.4).

Theoretically, modelling studies were initiated to account for the experimental data. A finite element program has been developed to describe the data over the entire sintering process. The sintering problem is considered as a special thermomechanical problem in which the instantaneous free strain rate as well as the material properties are density dependent. Experimental data for the relative density versus time for the composite is used to calculate the stresses that lead to a reduction in the densification rate. However, the density of the composite is not known a priori. The analysis has to be performed in an incremental fashion. The density calculated from the previous time step is used to calculate the instantaneous stress and the material parameters of the current time step. Both single inclusion and multiple inclusion cases have been considered.

Inhomogeneity in the matrix density has also been considered. The modelling studies are described in Section 2.3.

The main accomplishments of the experimental and theoretical research are summarized in Section 2.4.

The experimental and theoretical studies conducted in the first year of the present program are described in the following sections.

## **2.2 EXPERIMENTAL STUDIES**

### **2.2.1 Sintering of Model Ceramic Composites Formed by Conventional Processing**

#### **2.2.1(a) Experimental Procedure**

A fine grained ZnO powder (Reagent Grade, Mallinckrodt Inc., Paris, KY; average particle size  $\approx 0.3 \mu\text{m}$ ) was used as the matrix phase and the inclusion phase consisted of relatively coarse ZrO<sub>2</sub> particles (SC Grade, Magnesium Electron Inc., Flemington, NJ) with three different average sizes (1, 3, and 14  $\mu\text{m}$ ). The ZnO powder was the same as that used in earlier work of Rahaman and De Jonghe.<sup>1,14,15</sup> Composite samples containing up to 22.5 v% inclusions (based on the fully dense material) were formed by conventional processing techniques. The matrix powder and inclusions were mixed by milling in isopropanol in a polyethylene container using high purity zirconia balls as the milling medium. The mixture was then stir-dried and ground lightly with a mortar and pestle. Green composite bodies (6 mm in diameter by 6 mm) with a matrix density of  $0.51 \pm 0.01$  were formed by uniaxial pressing in a die at pressures of  $\approx 25 - 30$  MPa.

The compacted samples were sintered either under isothermal conditions at three fixed temperatures of 750, 850 and 950 °C, or at a constant heating rate of 4 °C/min. Most of the experiments were terminated after 3 h for isothermal sintering or 1200 °C for constant heating rate sintering, but additional samples were sintered for longer times (equivalent to higher temperatures for constant heating rate sintering) to produce composites with higher density. All experiments were performed in air in a dilatometer (Dilatronic 1600 °C, Theta Industries Inc., Port Washington, NY) that allowed continuous monitoring of the axial shrinkage. The composite density was measured from the axial shrinkage and the initial density. The density of the matrix phase of the composite was calculated from the

measured composite density using the method outlined earlier.<sup>14</sup> The final density of selected sintered samples were also checked by Archimedes method.

To provide samples for grain size measurements, sintering was performed for the appropriate time (isothermal sintering) or to the appropriate temperature (constant heating rate sintering). A different sample was used for each run. Data was obtained from scanning electron micrographs of polished and chemically etched surfaces. Dilute acetic acid was used as the etchant. The grain size was taken as 1.5 times the mean intercept length determined from about 50 measurements for each sample.

## 2.2.1(b) Results and Discussion

As outlined earlier, sintering experiments were performed either at a constant heating rate ( $4\text{ }^{\circ}\text{C}/\text{min}$ ) or isothermally. The results for the constant heating rate experiments will be considered first.

Figure 1 shows the data for the relative density of the composite matrix,  $\rho_m$  vs temperature for ZnO containing 0-22.5 v% ZrO<sub>2</sub> inclusions (average particle size  $\approx 14\text{ }\mu\text{m}$ ) during sintering to  $1200\text{ }^{\circ}\text{C}$ . Each curve is the average of two runs under identical conditions and the data are reproducible to within  $\pm 1\%$ . The increase in the volume fraction of the inclusions,  $v_i$ , caused a decrease in the density at any temperature. The composite density did not reach a limiting value when the unreinforced ZnO stopped densifying (at  $\approx 1100\text{ }^{\circ}\text{C}$ ); the density continued to improve at higher temperature.

The matrix densification rate,  $\dot{\epsilon}_m$ , equal to  $(1/\rho_m)d\rho_m/dt$ , was calculated from the data of Fig. 1 by fitting smooth curves to the data and differentiating; the results are shown in Fig. 2 as a function of temperature. Two temperature regimes are observed: one between  $\approx 650$  and  $950\text{ }^{\circ}\text{C}$  where the densification rate at any temperature decreased with increasing  $v_i$  and the other above  $\approx 950\text{ }^{\circ}\text{C}$  where the densification rate increased with increasing  $v_i$ .

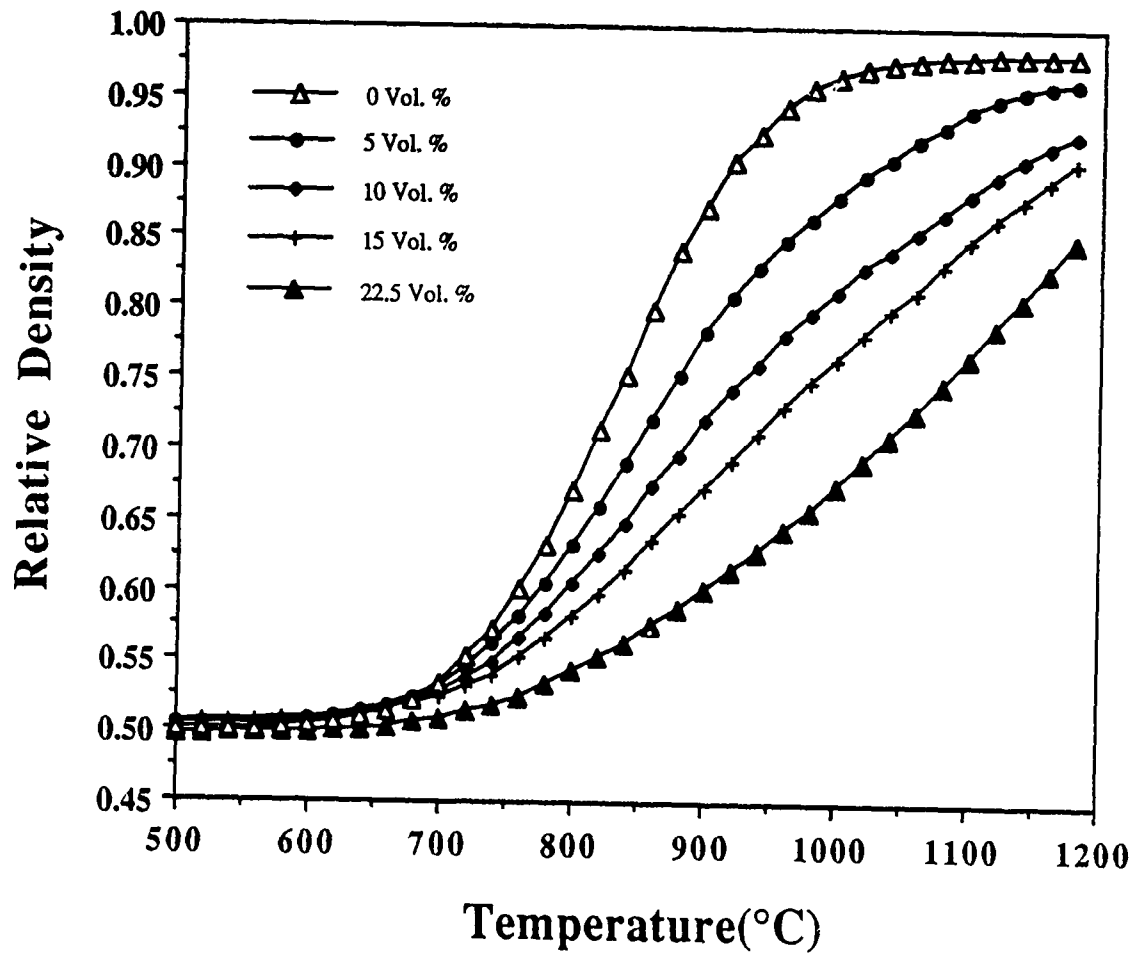


Fig. 1 : Matrix relative density versus temperature for conventionally processed ZnO containing 0-22.5 v% ZrO<sub>2</sub> (average size 14 microns) during constant heating rate sintering at 4°C/min. to 1200°C.

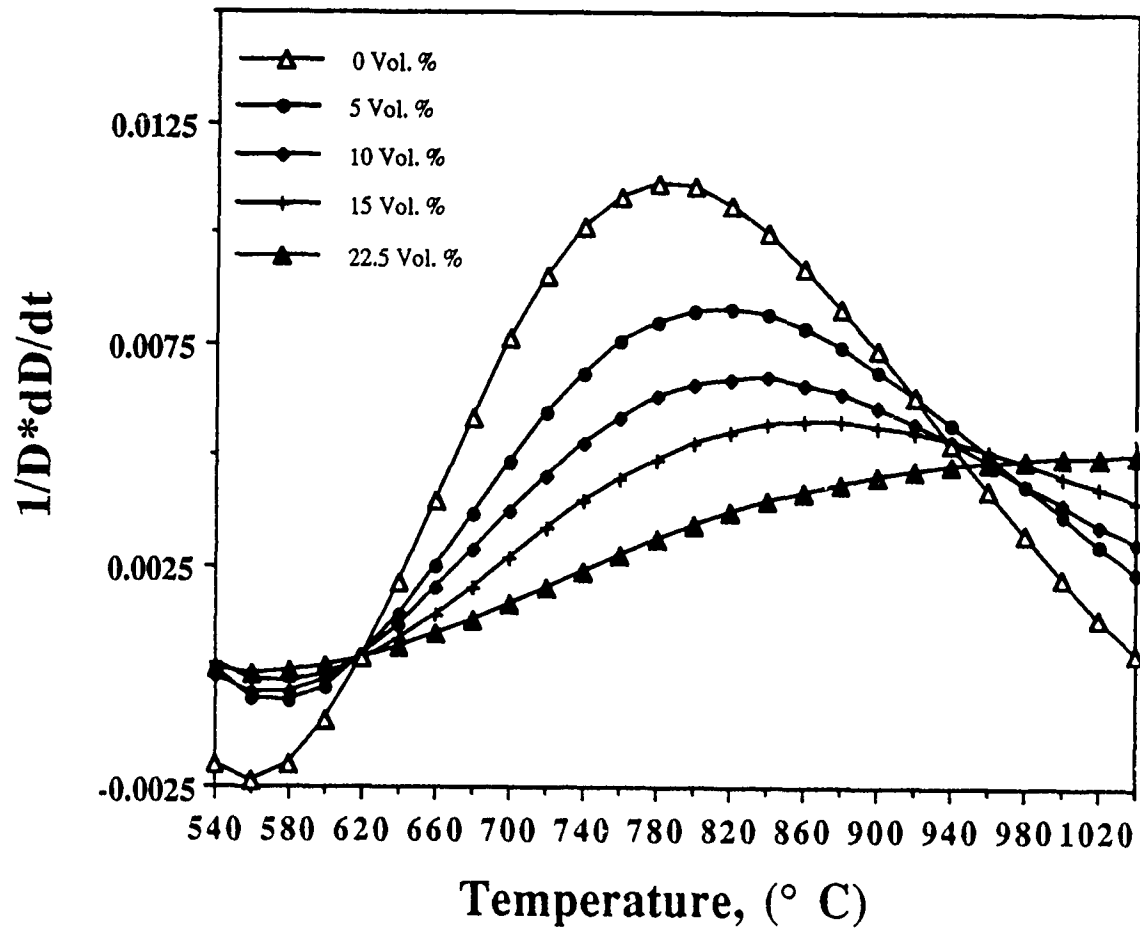


Fig. 2 : Matrix densification rate versus temperature for the composites described in Fig. 1.

Figure 3 shows the data for both  $\rho_m$  and the matrix grain size, G, for ZnO and a composite containing 10 v% ZrO<sub>2</sub>. It is seen that at any temperature, the inclusions caused a decrease in both  $\rho_m$  and G.

The data for G vs  $\rho_m$  is shown in Fig. 4 for ZnO and a ZnO/10 v% ZrO<sub>2</sub> composite. For  $\rho_m$  up to  $\sim 0.92$ , the grain size vs density relationship is approximately the same for ZnO and the composite. This is an interesting result and shows that the grain size of the matrix depends only on the density of the sample regardless of the temperature required to achieve that density.

The effect of inclusion size on the sintering of ZnO is shown in Fig. 5 for composites containing 10 v% ZrO<sub>2</sub> inclusions with average sizes of  $\sim 14$ , 3 and 1  $\mu\text{m}$ . The matrix density decreased with decreasing inclusion size. This decrease cannot be explained by current models.

For the isothermal sintering experiments, Fig. 6 shows the data for  $\rho_m$  vs time for ZnO and a ZnO/10 v% ZrO<sub>2</sub> composite at three different temperatures: 750, 850 and 950 °C. The inclusion size was 14  $\mu\text{m}$ . The composite reached a limiting density which was significantly lower than the density of the unreinforced sample. This behavior is qualitatively different from that observed earlier for the constant heating rate experiments where the matrix density increased with temperature and approached the value for the fully dense ZnO.

The G vs  $\rho_m$  data for isothermal sintering at 850 °C is shown in Fig. 7 for ZnO and a ZnO/10 v% ZrO<sub>2</sub> composite. The data for the composite is nearly identical to that for the unreinforced ZnO up to  $\rho_m \sim 0.80$ ; this value of  $\rho_m$  corresponded to the limiting density reached by the composite matrix. Further prolonged sintering caused very slow grain growth with almost no increase in density.

To compare the data from the isothermal and constant heating rate experiments, the ratio of the densification rate of the composite matrix,  $\dot{\epsilon}_m$ , to the densification rate of

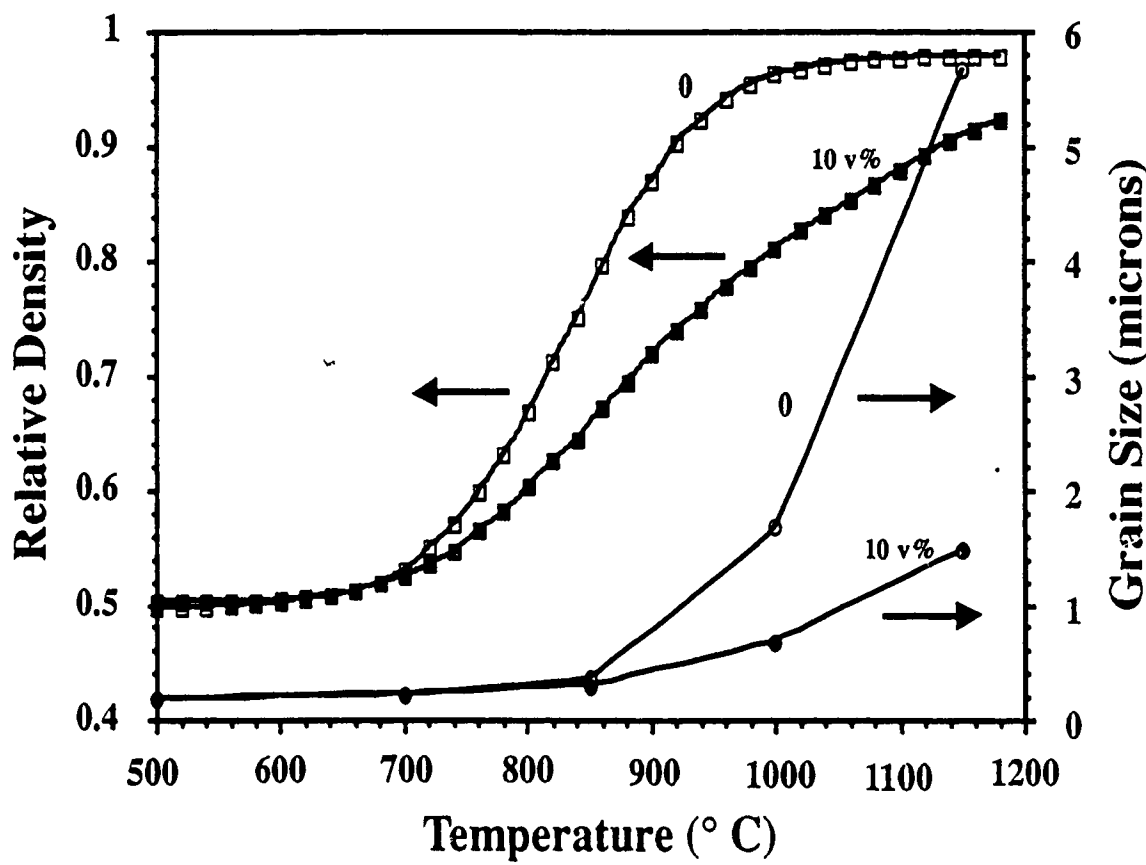


Fig. 3 : Matrix relative density and grain size versus temperature for ZnO and ZnO/10v% ZrO<sub>2</sub> composite during constant heating rate sintering at 4°C/min. to 1200°C.

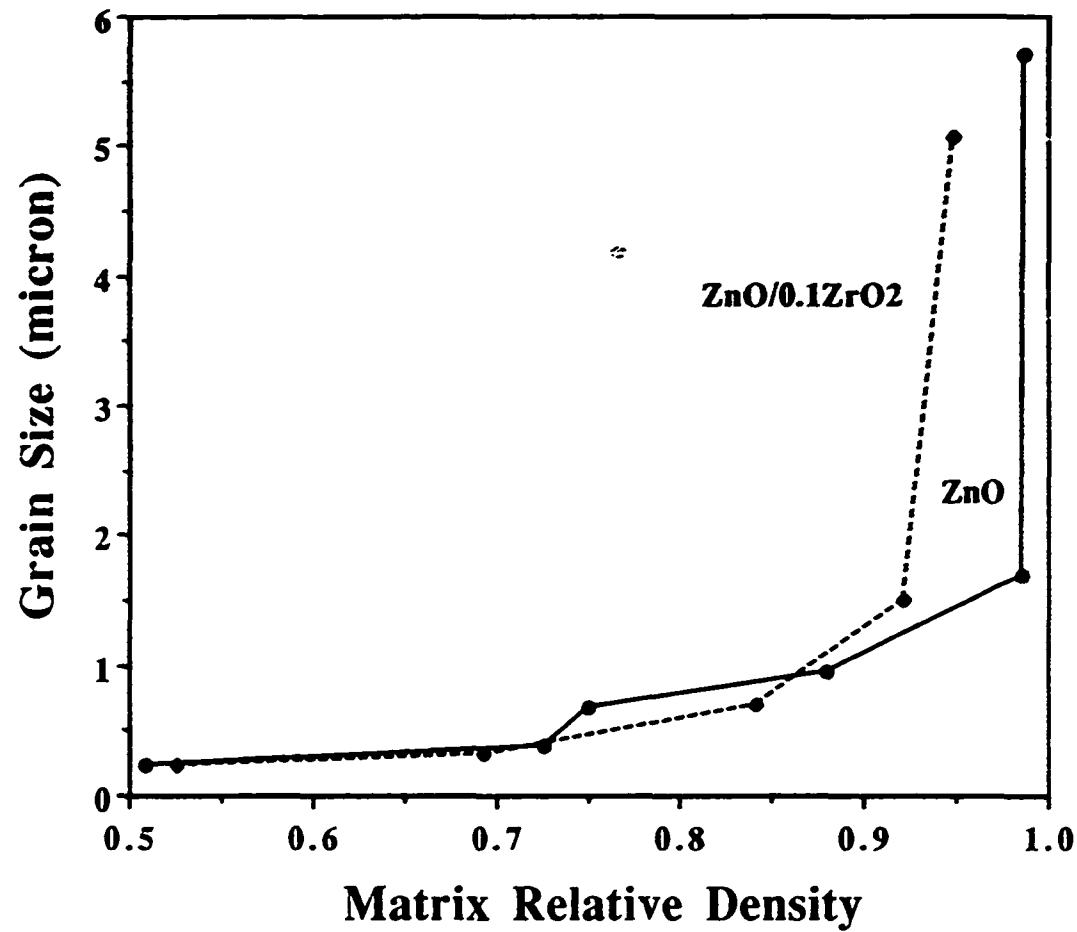


Fig. 4 : Grain size versus matrix density for ZnO and ZnO/10v%ZrO<sub>2</sub> composite during constant heating rate sintering.

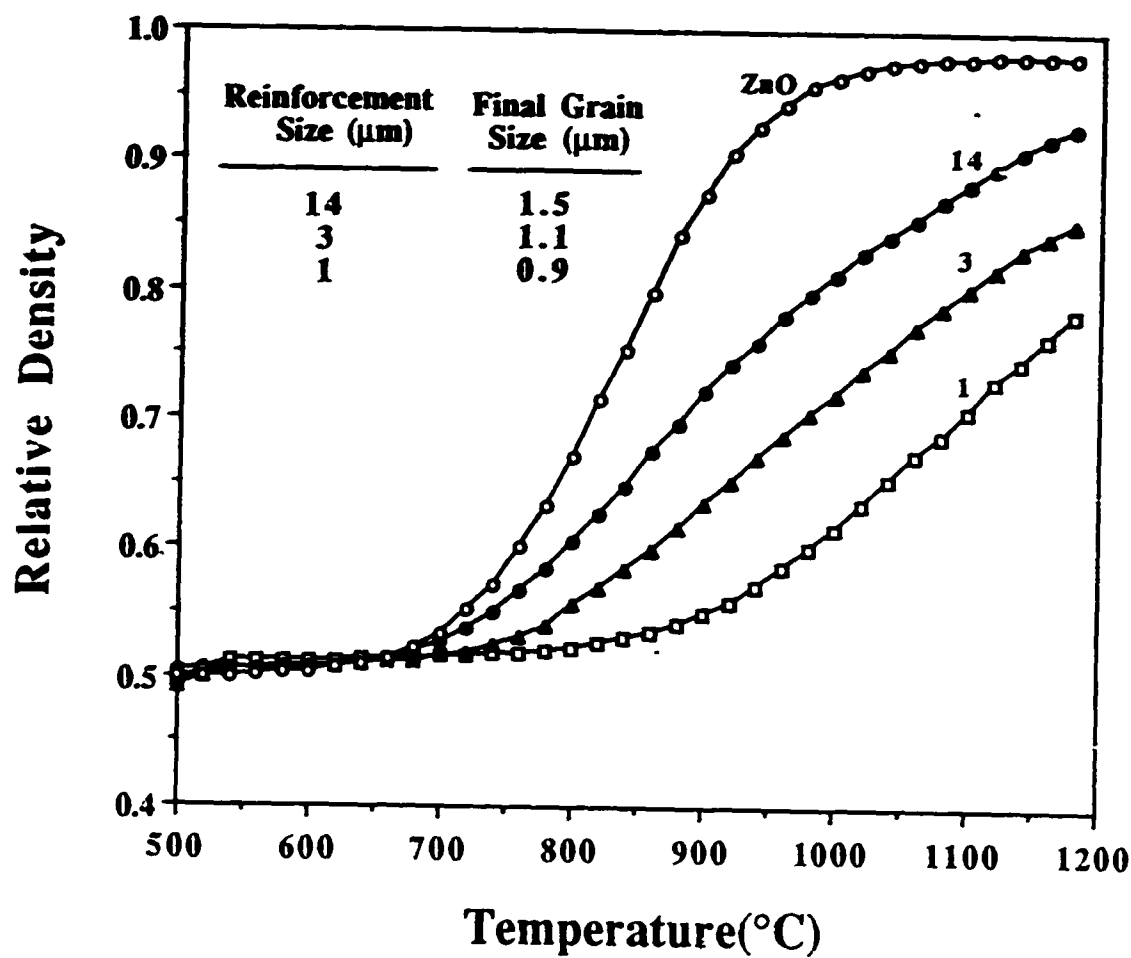


Fig. 5 : Matrix relative density versus temperature for ZnO and ZnO/10v%  $\text{ZrO}_2$  composite showing the effect of inclusion size.

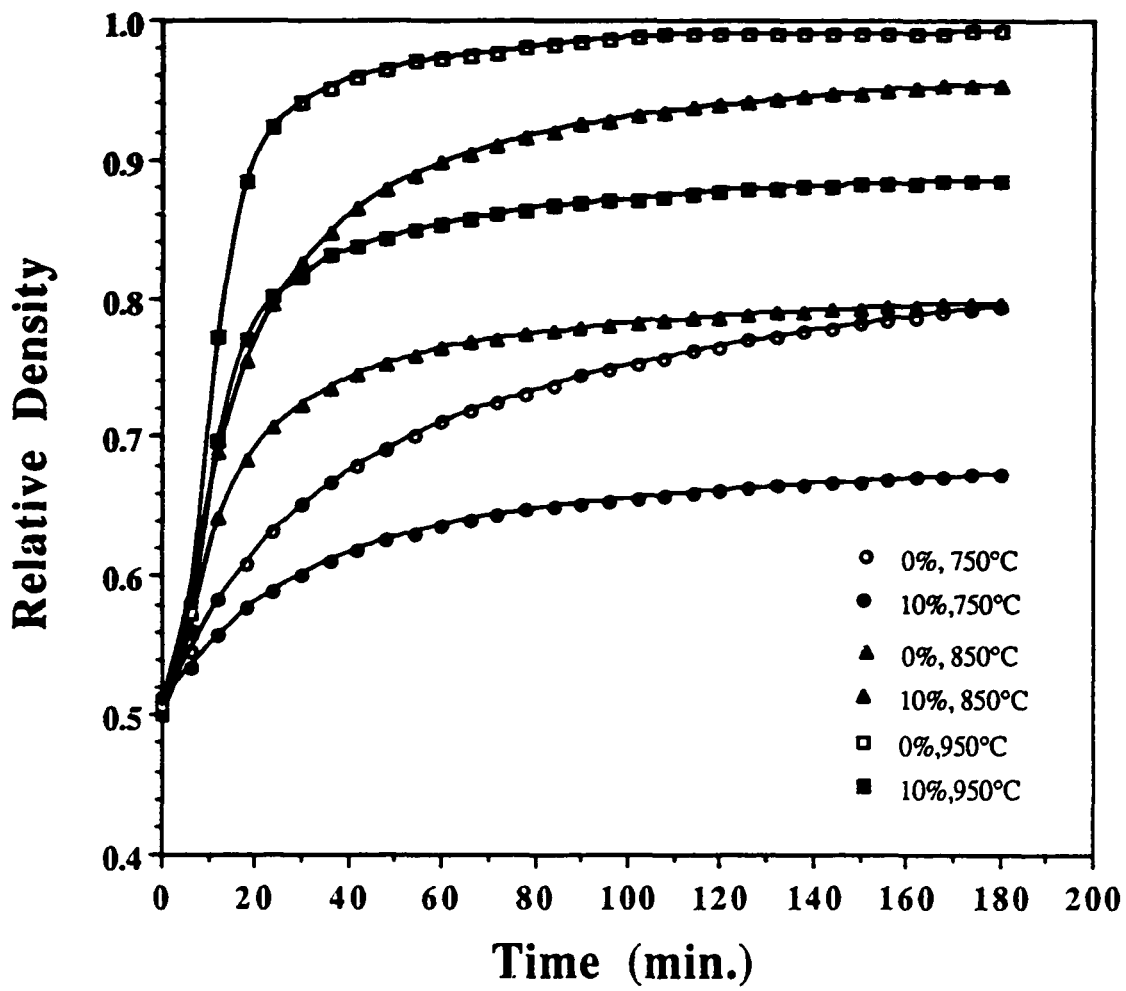


Fig. 6 : Matrix relative density versus time for ZnO and ZnO/10v% ZrO<sub>2</sub> composite during isothermal sintering at 750, 850, and 950°C

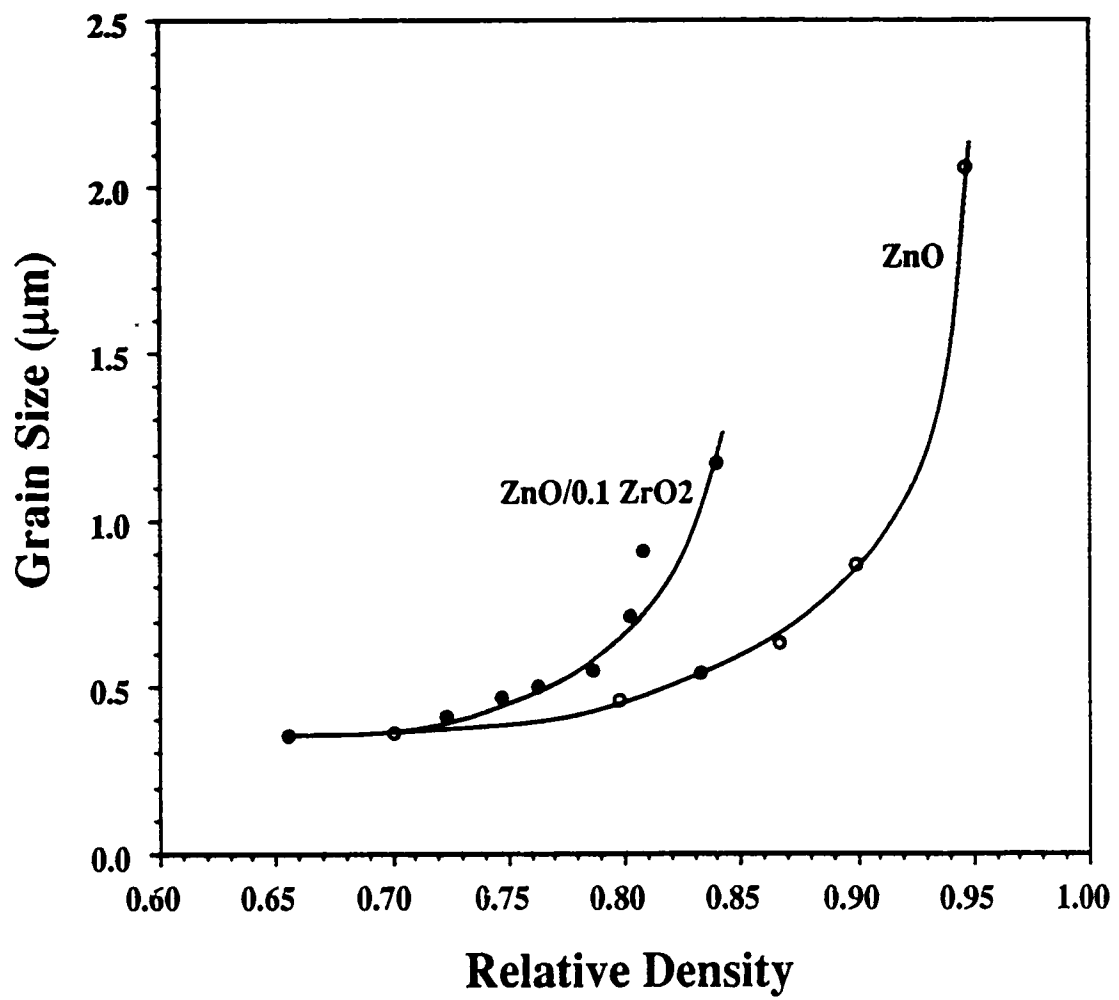


Fig. 7 Grain size versus matrix density for ZnO and ZnO/10v%ZrO<sub>2</sub> composite during isothermal sintering at 850°C.

the unreinforced ZnO,  $\dot{\epsilon}_u$ , is shown in Fig. 8 as a function of time (isothermal sintering) and as a function of temperature (constant heating rate sintering). The ratio  $\dot{\epsilon}_m/\dot{\epsilon}_u$  was almost constant with time (or density) but increased with the sintering temperature for isothermal sintering. The constant heating rate sintering data increased with temperature. As outlined recently,<sup>15</sup> the data of Fig. 8 can be expressed by:

$$\dot{\epsilon}_m \sim F \dot{\epsilon}_u \quad (1)$$

where  $F$  is factor that is strongly dependent on temperature but is weakly dependent on the matrix density. The increase in  $F$  with temperature indicates that improved processing conditions for ceramic composites should prevail at increased sintering temperatures. The temperature dependence of  $F$  does not follow from a treatment of the viscous backstress in a concentric sphere model for a densifying composite.<sup>5</sup> Instead it indicates that an additional process is involved that is strongly dependent on temperature.

Scanning electron micrographs of (a) the unreinforced ZnO and (b) a ZnO/10 v% ZrO<sub>2</sub> composite which were sintered under identical conditions (4 °C/min to 1200 °C) are shown in Fig. 9. The ZnO is almost fully dense with a nearly equiaxed microstructure. In contrast, the composite is highly porous with the porosity situated in two distinct regions: (i) immediately surrounding the inclusion particles and (ii) nearly evenly distributed within the bulk of the matrix. Figure 10 is a low magnification micrograph of the composite in Fig. 9(b) and shows the general distribution of the porosity immediately surrounding the inclusions.

The sintering data and the micrographs described earlier indicate that the reduced sinterability of the composite is due to two main factors: one that leads to highly porous regions immediately surrounding the inclusion particles, and the other that produces a reduction in the density (and grain size) in the bulk of the matrix phase. The first factor appears to be gross packing inhomogeneities near the inclusions due to inefficient mixing between the matrix powder and the inclusion particles. The second appears to be a

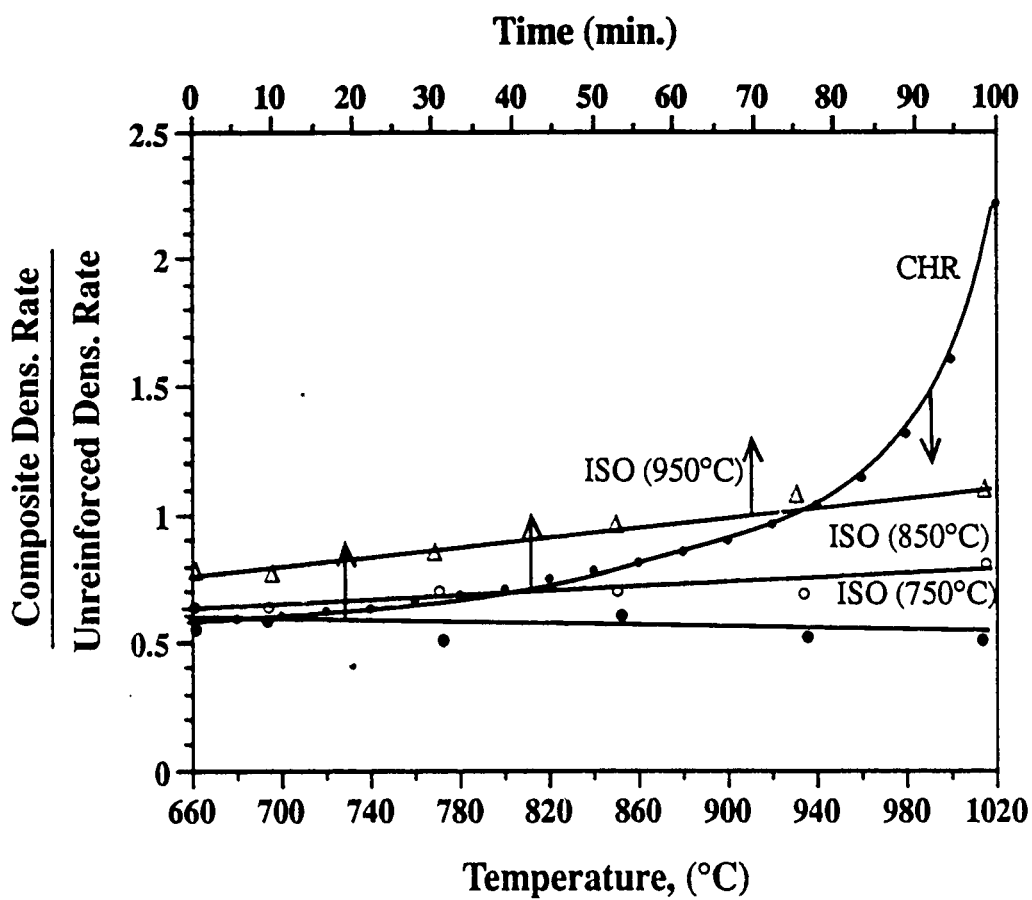
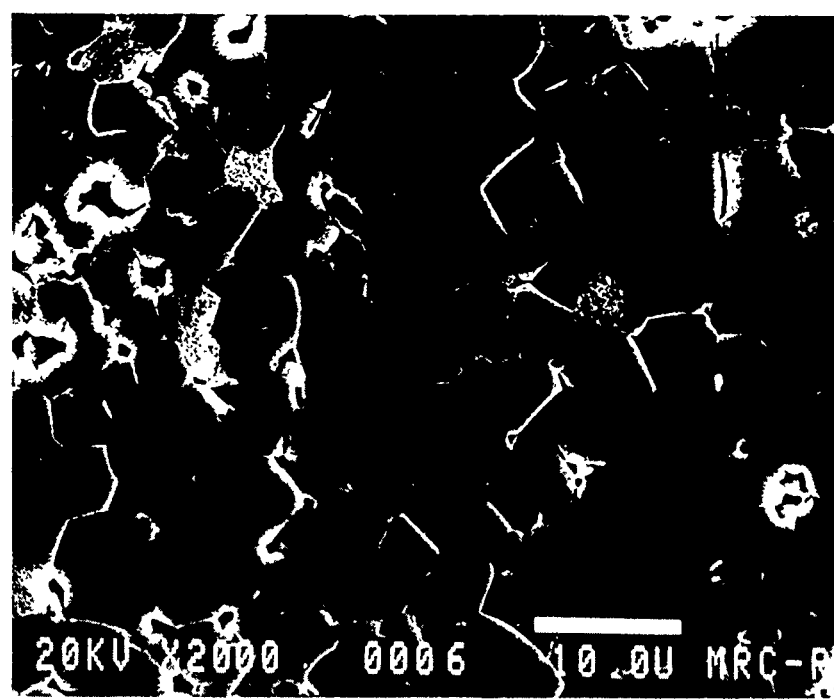
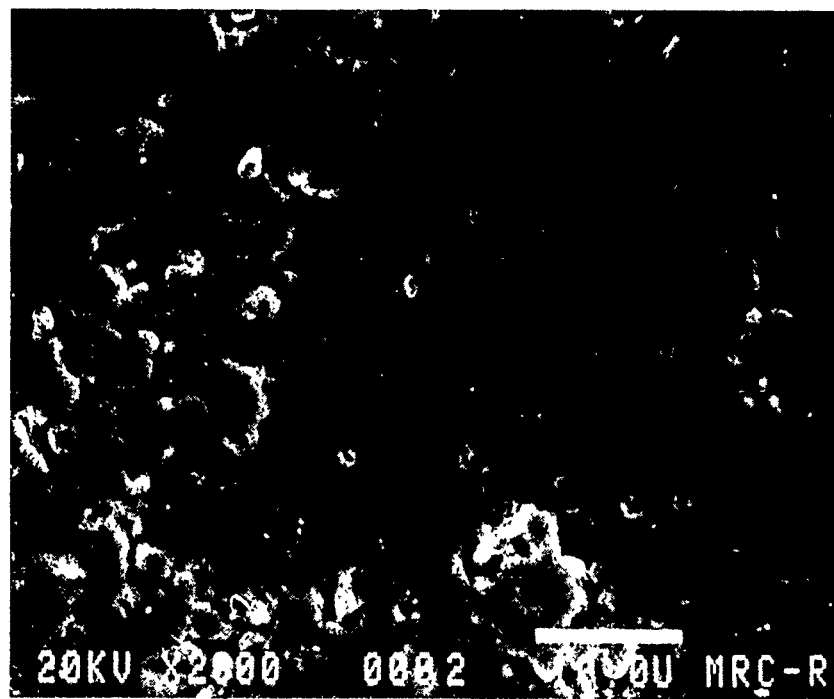


Fig. 8 : Ratio of the matrix densification rate for the  $\text{ZnO}/10\text{v\% ZrO}_2$  composite to the densification rate for unreinforced  $\text{ZnO}$  versus time (isothermal sintering) or versus temperature (constant heating rate sintering).



(a)



(b)

Fig. 9 : Scanning electron micrographs of (a) ZnO and (b) ZnO/10v% ZrO<sub>2</sub> composite, sintered under identical conditions (4°C/min. to 1200°C). The green bodies were formed by conventional processing.

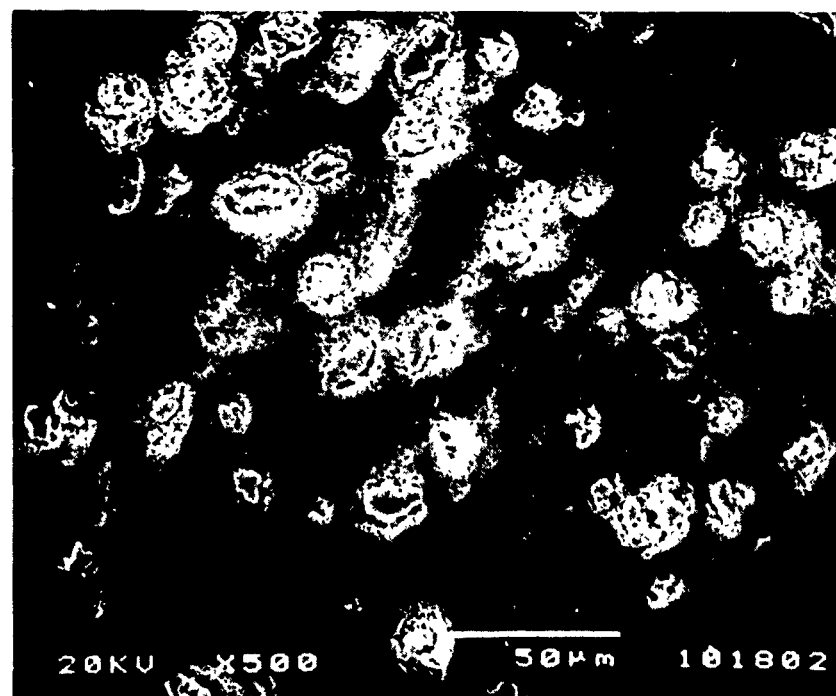


Fig. 10 : Low magnification scanning electron micrograph of the ZnO/10v%  $\text{ZrO}_2$  composite of Fig. 9(b), showing regions of higher porosity around the inclusions.

constraint on the matrix phase due to the inclusions; this constraint causes a reduction in the sintered density (or an increase in the porosity) of the composite matrix relative to the unreinforced matrix. Since the grain size of the matrix is controlled primarily by the density, as observed earlier, therefore the lower matrix density leads to a lower grain size. While the exact nature of the constraint on the matrix phase is, as yet, unknown, experiments in the present research program indicate that it may be due to particle-particle interactions between the inclusions (see Section 2.2.4: Effect of Rigid Inclusions on the Sintering and Viscosity of Glass).

In summary, the work outlined so far indicates that improved sintering of ceramic composites should be achieved with:

- (i) the use of higher sintering temperatures, and
- (ii) processing techniques which maximize the packing of the matrix powder around the inclusion phase, and which reduce the constraint on the matrix phase due to the inclusion particles.

## 2.2.2 Sintering of Model Ceramic Composites Formed by Slip Casting

### 2.2.2(a) Experimental Procedure

The matrix powder, ZnO, and the inclusion particles, ZrO<sub>2</sub>, were the same as those used earlier for the composites formed by conventional processing (i.e. Section 2.2.1). The ZnO powder and the ZrO<sub>2</sub> inclusions (average particle size  $\sim$  14 or 3  $\mu\text{m}$ ) were dispersed in water at a pH of 8.5 to produce a slurry with a solids content of  $\sim$  80 w%. Darvan 811 was used as a dispersant. The slurry was cast into gypsum molds to produce samples (6 mm in diameter by 6 mm) for sintering. The sintering experiments and microstructural observations were performed in the same way as described earlier for the conventionally processed composites.

### 2.2.2(b) Results and Discussion

Figure 11 shows the data for the matrix relative density vs temperature for the unreinforced ZnO and a ZnO/10 v% ZrO<sub>2</sub> composite during constant heating rate sintering at 4 °C/min to 1300 °C. Compared to the conventionally processed bodies, the unreinforced ZnO started densifying at a somewhat higher temperature; this difference in the sintering behavior may be due to a small amount of hydrolysis of the ZnO during slip casting. Since the green bodies were formed by a nearly identical process, therefore the effect of this hydrolysis would be expected to affect the unreinforced matrix and the composite in approximately the same way. The unreinforced ZnO body eventually reached nearly full density at  $\sim$  1250 °C. It is seen from Fig. 11 that the matrix density of the composite at any temperature is much lower than for the unreinforced ZnO. The highly reduced density of the composite matrix is comparable to the reduction observed for the conventionally

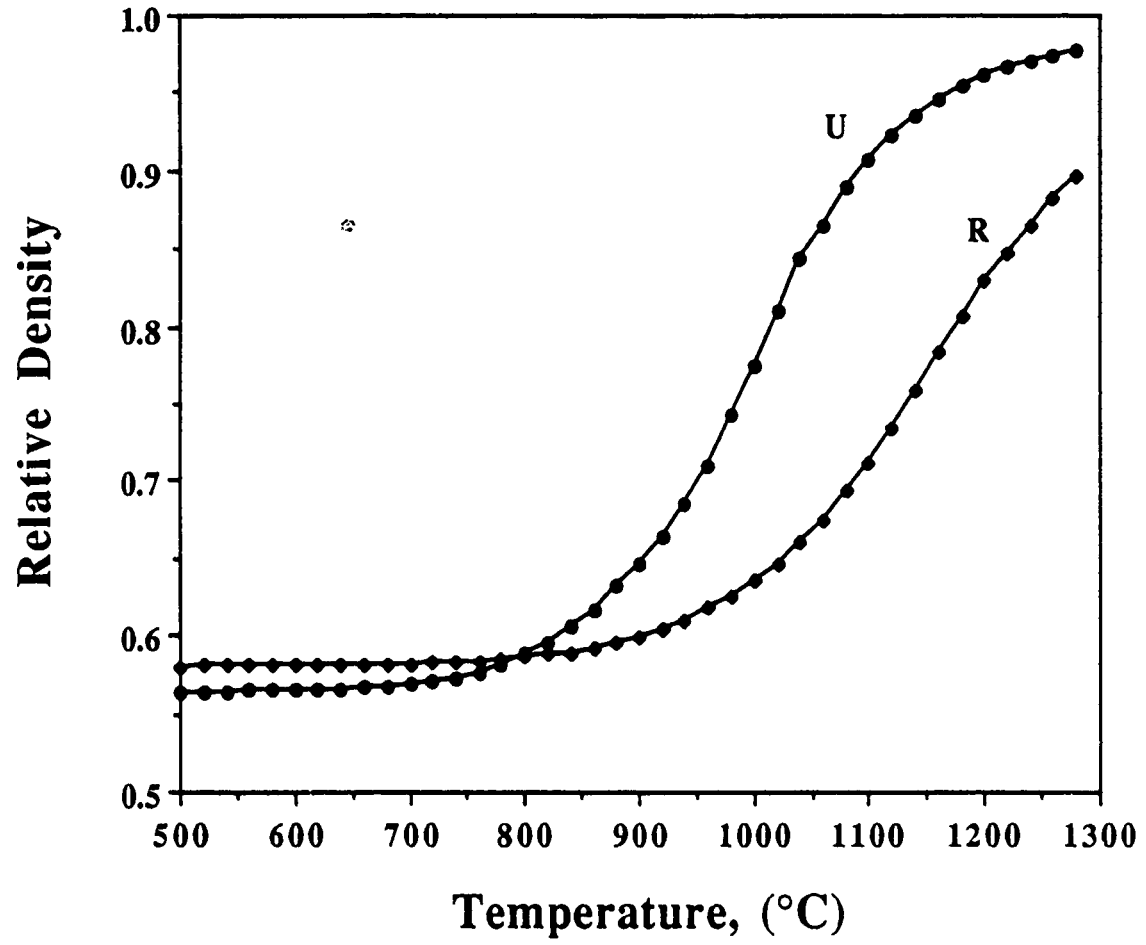


Fig. 11 : Matrix relative density for slip cast ZnO and ZnO/10v% ZrO<sub>2</sub> composite during constant heating rate sintering at 4°C/min. to 1300°C.

processed samples.

The ratio of the matrix densification rate of the composite to the densification rate of the unreinforced ZnO (i.e.  $\dot{\epsilon}_m/\dot{\epsilon}_u$ ) as a function of temperature is shown in Fig. 12. The curve has almost the same shape but is shifted to somewhat higher temperatures compared to the results for the conventionally processed bodies (Fig. 8).

Scanning electron micrographs of (a) the unreinforced ZnO and (b) a ZnO/10 v% ZrO<sub>2</sub> composite which were sintered under identical conditions (4 °C/min to 1300 °C) are shown in Fig. 13. It is seen that (i) the composite matrix is more porous than the unreinforced sample and (ii) the packing of the matrix phase close to the inclusions is much better compared to the conventionally processed composites (Fig. 9).

The kinetic data indicate that the sinterability of the slip cast composites is not significantly improved compared to the conventionally processed composites. However, the packing uniformity of the matrix phase immediately surrounding the inclusion particles is much improved. It is worth comparing the green composite microstructure expected from the conventional processing and slip casting routes. Both conventional processing and slip casting are expected to lead to a random distribution of the inclusion particles within the matrix. Slip casting is, however, expected to produce better packing uniformity of the matrix phase close to the inclusions and in the rest of the matrix. The feature that is common to both processing techniques, therefore, is the random distribution of the inclusion particles within the matrix. Hence, for the slip cast bodies, particle-particle interactions that result from the random distribution of the inclusion phase might be the main factor causing the reduced sinterability of the slip cast samples. For conventionally processed composites, an additional factor is the packing uniformity around the inclusion phase.

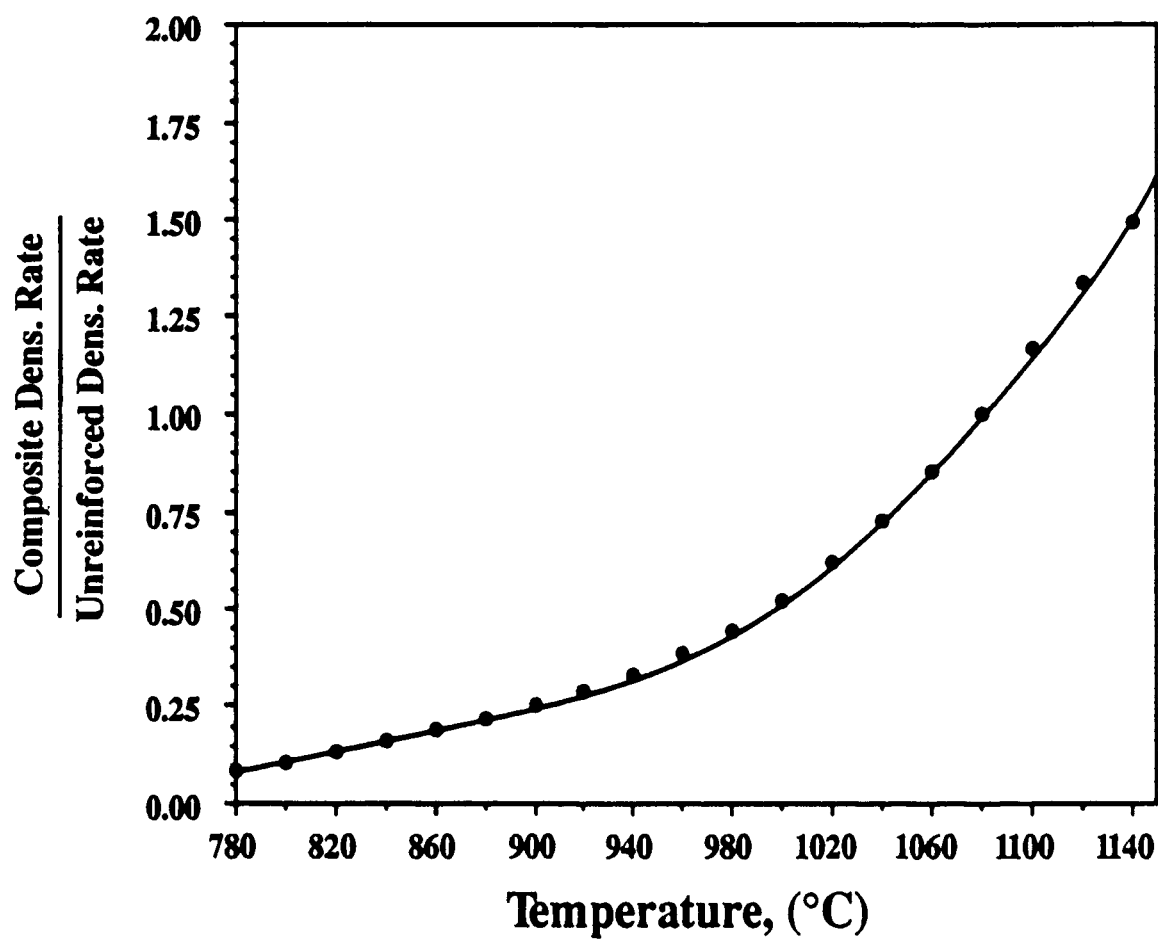
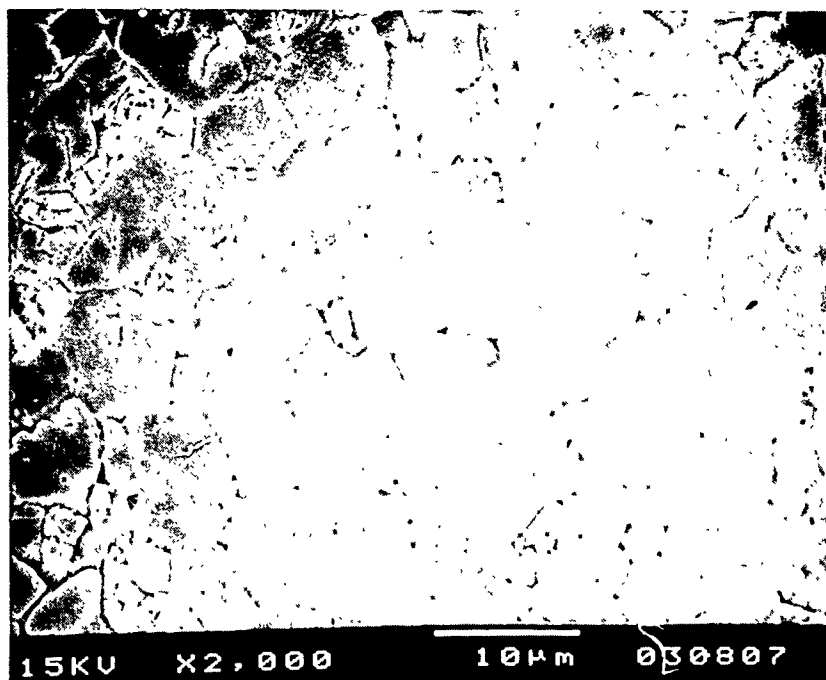
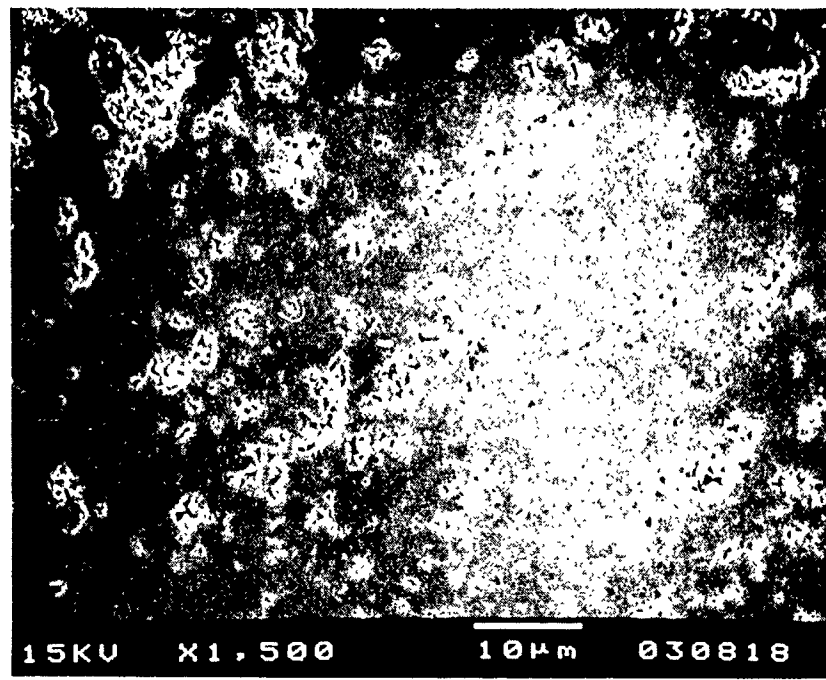


Fig. 12 : Ratio of the matrix densification rate for the slip cast ZnO/10v% ZrO<sub>2</sub> composite to the densification rate of the unreinforced ZnO versus temperature.



(a)



(b)

Fig. 13 : Scanning electron micrographs of (a) ZnO and (b) ZnO/10v% ZrO<sub>2</sub> composite, sintered under identical conditions . The green bodies were formed by slip casting.

### 2.2.3 Sintering of Model Ceramic Composites Formed from Coated Particles

As outlined earlier, the data for the conventionally processed composites and slip cast composites indicate that the matrix powder packing immediately surrounding the inclusions and particle-particle interactions between the inclusion particles (which are randomly distributed in the matrix) might be the important factors responsible for the reduced sinterability of ceramic particulate composites. The objective of this phase of the experimental work was to investigate whether these problems can be alleviated by improved processing. The forming method described in this section involved coating the individual inclusion particles with a cladding of the matrix powder by chemical precipitation, followed by die-pressing of the coated particles.

#### 2.2.3(a) Experimental Procedure

The ZrO<sub>2</sub> inclusion particles (average size 14, 3 and 1  $\mu\text{m}$ ) were the same as those used earlier in the formation of composites by conventional processing and by slip casting. The inclusion particles were coated with a matrix phase of ZnO by chemical precipitation. In the coating process, the ZrO<sub>2</sub> particles were dispersed in a solution of zinc chloride and urea (Aldrich Chemical Company) at a pH of 6.7. All solutions were prepared in distilled water. The system was aged at 70 °C with continuous stirring for  $\sim$  20 hours, cooled to room temperature and the solids were recovered by filtration. After washing with distilled water, the solids were dried at 150 °C for 24 hours. Coated particles containing up to  $\sim$  40 v% inclusion particles (based on the fully dense composite) were synthesized. For comparison, pure ZnO powder (i.e. containing no inclusion particles) was synthesized by the same chemical precipitation process.

The powders were compacted by uniaxial pressing in a die to produce green bodies with

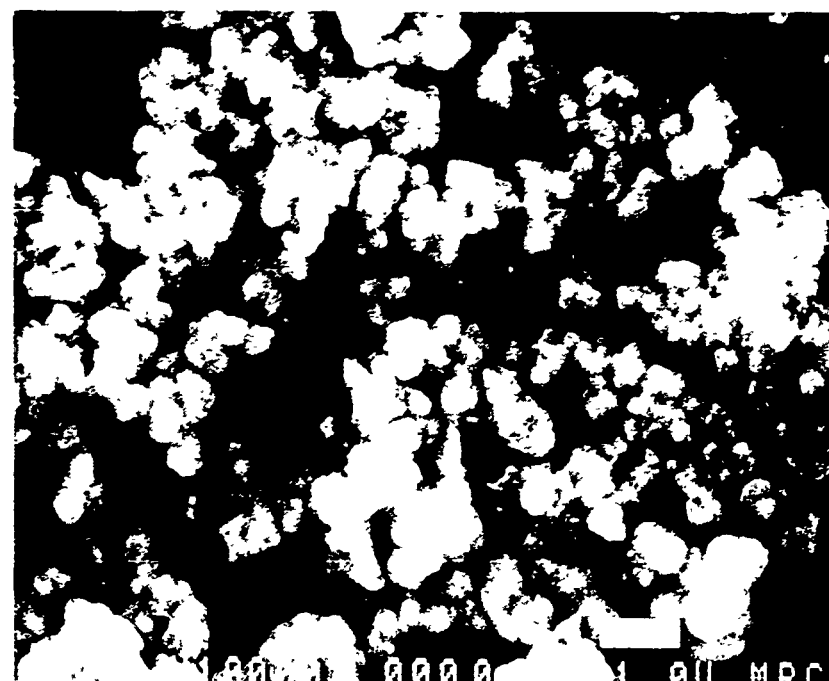
approximately the same matrix density ( $0.52 \pm 0.02$ ). The compacts were sintered in air at a constant heating rate of  $4\text{ }^{\circ}\text{C}/\text{min}$  to  $1500\text{ }^{\circ}\text{C}$  in the dilatometer used earlier.

### 2.2.3 Results and Discussion

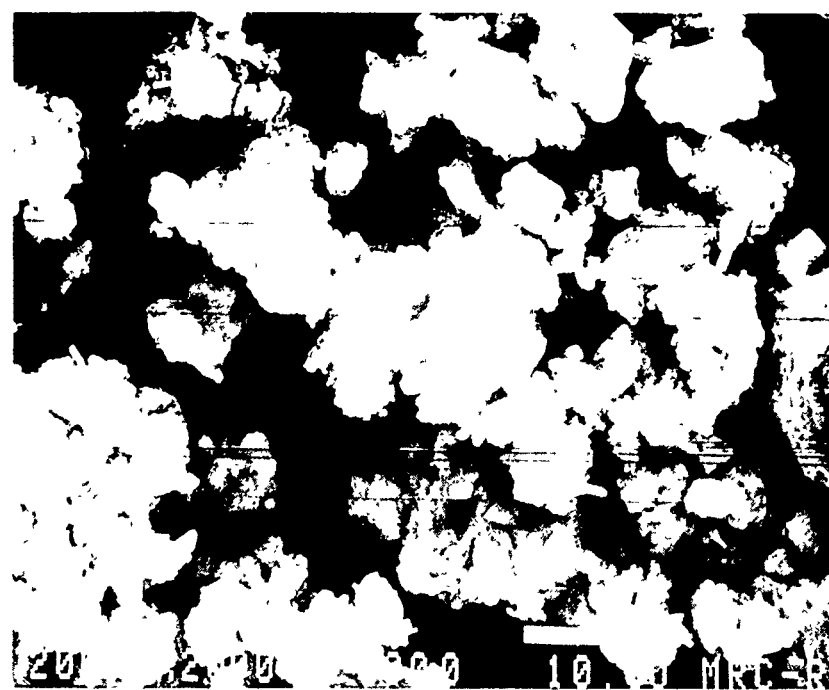
Figure 14 shows scanning electron micrographs of (a)  $\text{ZrO}_2$  inclusion particles with an average size of  $\sim 3\text{ }\mu\text{m}$ , and (b) the same particles after they were coated with  $\text{ZnO}$  powder by chemical precipitation. The coated particles appear somewhat agglomerated. X-ray diffraction and energy dispersive X-ray analysis in the scanning electron microscope for coated particles containing 20 v% of the inclusion phase did not reveal the presence of the  $\text{ZrO}_2$  inclusions. This is a strong indication that the inclusion particles were indeed coated by the  $\text{ZnO}$  matrix phase. As a further check, high voltage transmission electron microscopy will be used in future work.

The matrix relative density versus temperature for the composites formed from coated particles is shown in Fig. 15. The  $\text{ZrO}_2$  inclusion size was  $\sim 3\text{ }\mu\text{m}$ . For comparison, the data for the  $\text{ZnO}$  precipitated under the same conditions as the coated particles is also shown. The pure  $\text{ZnO}$  started to densify at a higher temperature compared to the commercial  $\text{ZnO}$  powder (particle size  $\sim 0.3\text{ }\mu\text{m}$ ) used for the conventionally processed samples. Although the particle size of the chemically precipitated powder has not, as yet, been measured, the difference in sintering characteristics between the two  $\text{ZnO}$  powders might be related to a difference in particle size. The data of Fig. 15 show that composites with up to 35 v% of inclusions densified to nearly full density under identical conditions used for the unreinforced matrix which reached a density of only 0.93. Further, the densification of the matrix is rather insensitive to the inclusion volume fraction for the range studied.

Figure 16 shows data for the matrix density as a function of time for composites with



(a)



(b)

Fig.14 : Scanning electron micrographs of (a) ZrO<sub>2</sub> inclusion particles and (b) coated particles.

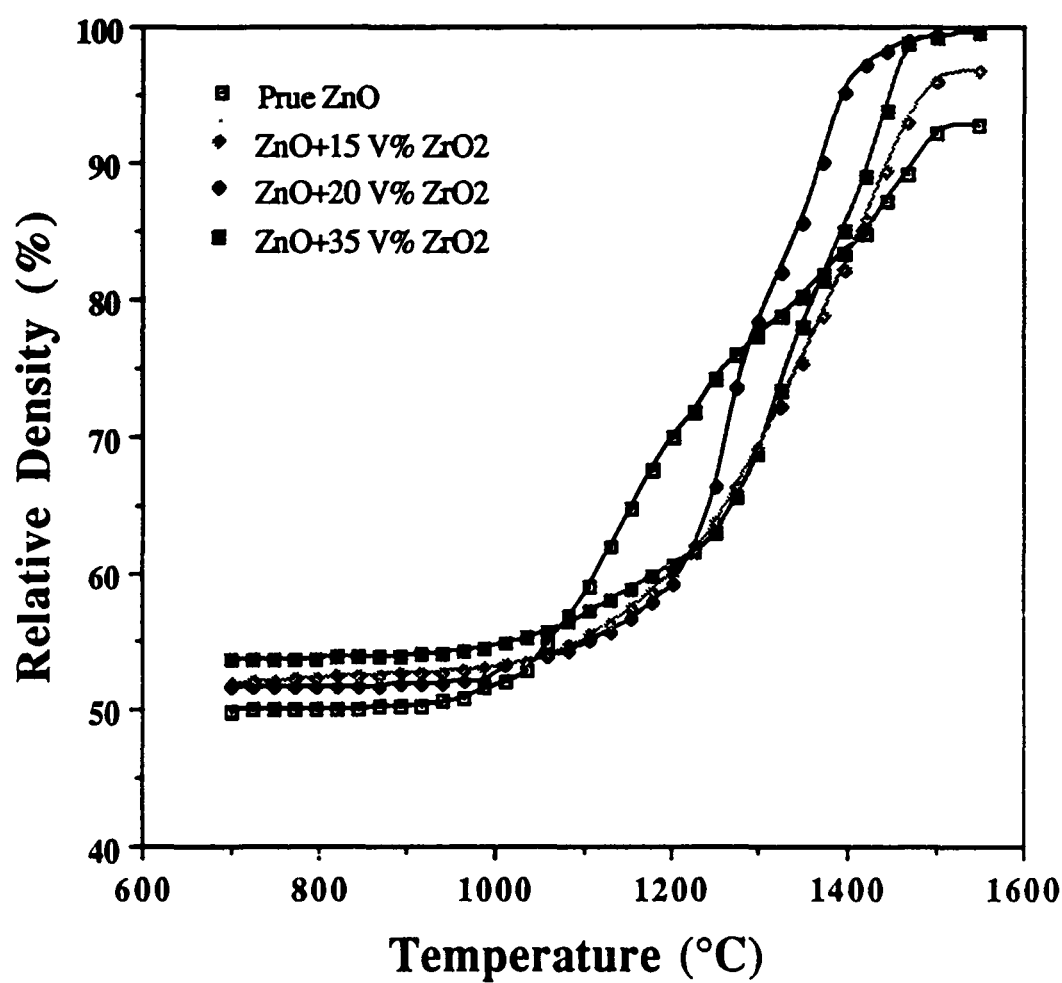


Fig.15 : Matrix relative density versus temperature for ZnO and ZnO containing up to 35 V% ZrO<sub>2</sub> inclusions ( particle size 3 micron) during constant heating rate sintering. The composites were formed from coated particles.

a fixed inclusion content (20 v%) but with different inclusion sizes of 14, 3 and 1  $\mu\text{m}$ . It is seen that the inclusion size has almost no effect on the densification of the matrix.

The insensitivity of the matrix densification to inclusion content and inclusion size (Figs. 15 and 16) is remarkably different from the data for the conventionally processed bodies and for the slip cast bodies. The results show very clearly that the effects of rigid inclusions on the sintering of ceramic composites are processing-related.

Figure 17 shows scanning electron micrographs of (a) a polished surface and (b) a fractured surface of a composite containing 20 v% inclusions (particle size 3  $\mu\text{m}$ ) that was formed from coated particles and sintered at 4  $^{\circ}\text{C}/\text{min}$  to 1500  $^{\circ}\text{C}$ . It is seen that the matrix (including the region immediately surrounding the inclusions) is nearly fully dense. The fractured surface shows that the matrix consists of nearly equiaxed grains.

In summary, the results for the composites formed from coated powders show that the problems associated with the sintering of ceramic composites can be alleviated by the present technique of coating the inclusion particles with the matrix. Since the main advantages of this method are (i) the improvement of the matrix packing immediately surrounding the inclusions and (ii) reduction in the particle-particle interactions between the inclusions, therefore the data provide further evidence that non-uniform packing of the matrix immediately surrounding the inclusions and inclusion particle interactions are the main factors responsible for the reduced densification rates in conventionally processed composites. Slip casting leads to an improvement in the matrix packing immediately surrounding the inclusions (compared to conventional processing) but the interactions between the inclusion particles are not significantly reduced.

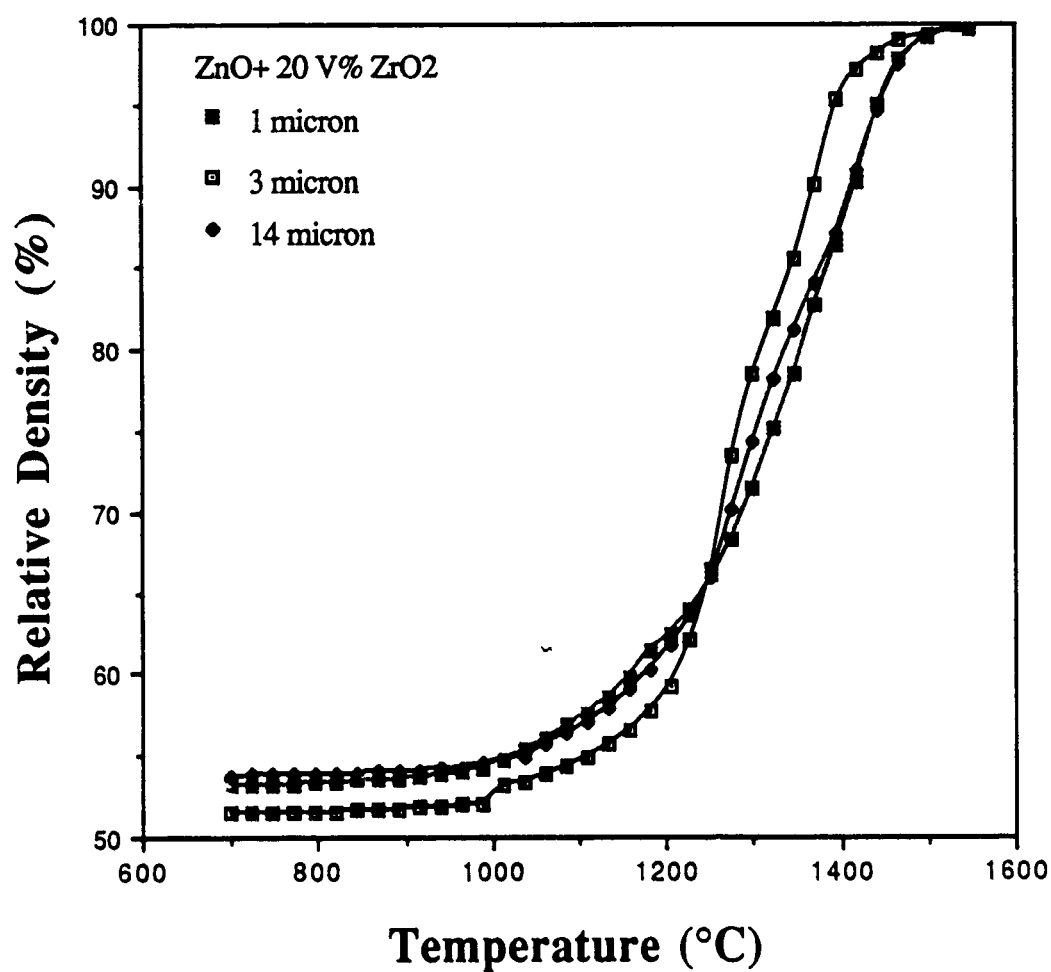
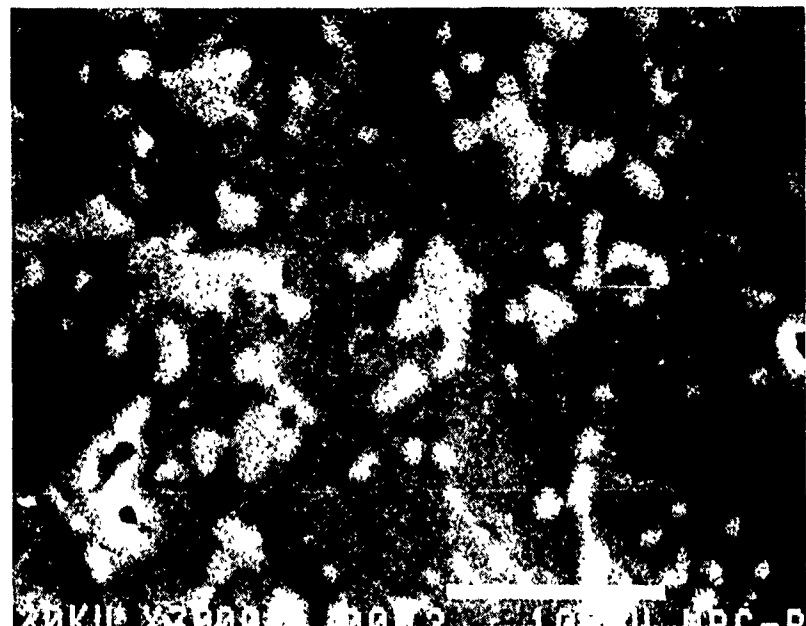
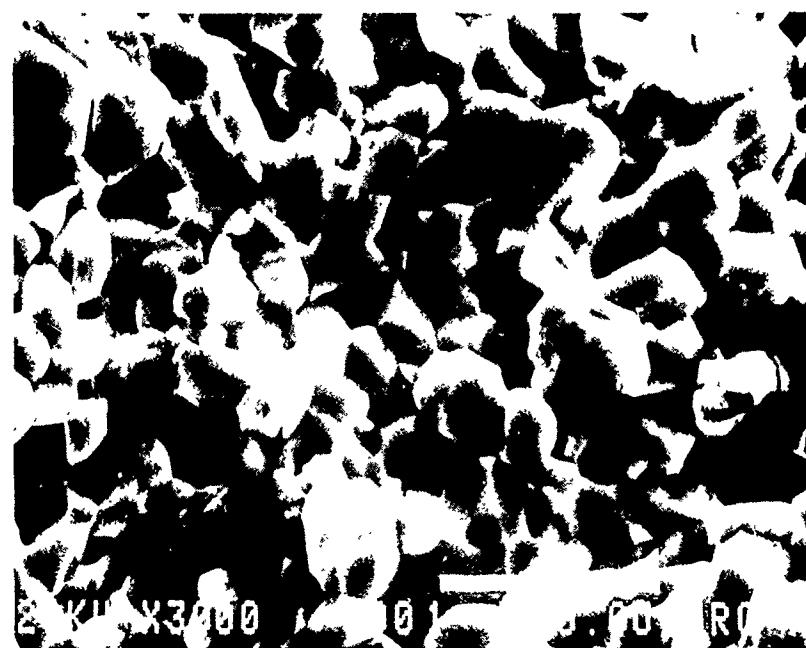


Fig.16 : Matrix relative density versus temperature for ZnO/20 V% ZrO<sub>2</sub> composites formed from coated particles, showing almost no effect of the ZrO<sub>2</sub> inclusion size.



(a)



(b)

Fig.17 : Scanning electron micrographs of (a) a polished surface and (b) a fractured surface of a ZnO/20 V% ZrO<sub>2</sub> composite formed from coated particles and sintered at 4°C / min. to 1485°C.

#### 2.2.4 Effect of Rigid Inclusions on the Composite Viscosity

The experiments described earlier indicated that interactions between the inclusion particles provide an important barrier to the sintering of composites formed by conventionally processing and by slip casting. Significant interactions between the inclusion particles should lead to an increase in the viscosity of the composite. An important issue therefore is the effect of the inclusion phase on the viscosity of the composite. The dependence of the composite viscosity on the volume fraction and size of the inclusion phase can provide insight into the importance of inclusion-inclusion and inclusion-matrix interactions and how these affect sintering. Since the sintering of glass matrix composites is qualitatively different from that for polycrystalline composites, it is also important to determine whether the effect of an inclusion phase on the viscosity of a glass matrix is different from that for a polycrystalline matrix. In the first phase of these experiments, the effect of spherical nickel particles on the viscosity of a soda-lime glass matrix composite was measured. Glass was chosen as the matrix phase for the initial phase of this study to eliminate the complexities of grain growth. Current work is examining the effect of  $ZrO_2$  inclusions on the viscosity of a  $ZnO$  matrix composite and the results will be reported later.

##### 2.2.4(a) Experimental Procedure

Spherical soda-lime glass powder (diameter 10-20  $\mu m$ ; MOSCI Corporation, Rolla, MO) was used as the matrix phase and the inclusion phase consisted of nearly spherical Ni particles with three different size ranges: 6-10, 100-150, and 150-300  $\mu m$  (Johnson Matthey, Ward Hill, MA). The glass powder and inclusion particles were mixed in methanol and stir-dried. Approximately 5 v% of carbowax was used as a binder. For comparison, the

pure glass powder was subjected to the same mixing treatment. The powders were then pressed uniaxially in a die to form samples (6 mm in diameter by 6 mm) with a matrix relative density of  $\sim 0.60$ . The compacted samples were heated slowly to  $\sim 400$  °C to remove the binder and then presintered in argon gas at 4 °C/min to 710 °C to produce compacts with sufficient green strength for manipulation in the dilatometer. All samples were given the same binder burnout and presintering treatment. The presintering treatment resulted in an increase of 2-3% in the relative density of the sample.

The unreinforced glass and composite samples were sintered isothermally with or without load in argon gas at 730 °C in a loading dilatometer<sup>16,17</sup> that allowed continuous monitoring of the axial shrinkage. For sintering with load, the initial stress on the compact was 18 kPa. The density, creep strain and creep viscosity during sintering were determined from the data using a procedure outlined earlier.<sup>16,17</sup>

In a separate set of experiments, the creep behavior of nearly fully dense glass and composite samples were also measured. The compacts were first sintered freely (i.e. without load) at 730 °C to nearly full density. In the creep experiments, a sample was placed in the loading dilatometer and after the desired temperature (730 °C) had been reached, a stress of 18 kPa was applied. The axial strain of the sample was measured as a function of time.

Microstructural observations of the samples various stages of sintering were performed by scanning electron microscopy.

## 2.2.4(b) Results and Discussion

Figure 18 shows the data for the matrix relative density versus time for the unreinforced glass and glass matrix composites containing 10 v% Ni inclusions during sintering at 730 °C. (The load on the samples was  $\sim 3$  kPa, corresponding to the load

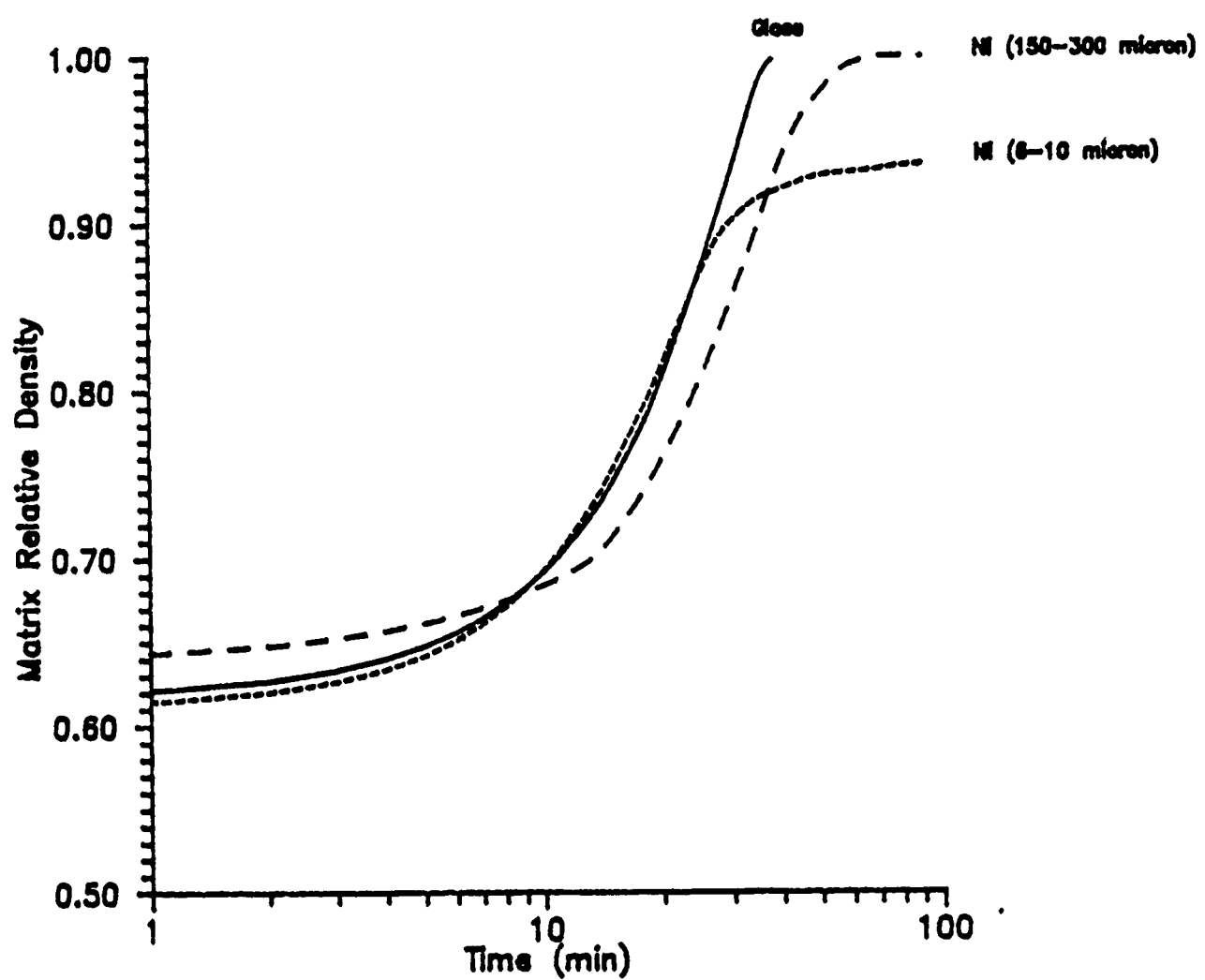


Fig.18 : Matrix relative density versus time for glass and glass matrix composites containing 10 V% Ni particles sintered at 730°C under a uniaxial load of 3 kPa.

required to maintain contact of the dilatometer pushrod on the sample). These density data were calculated from the measured axial strain data using the procedure outlined earlier.<sup>16,17</sup> The size of the Ni inclusions was 6-10  $\mu\text{m}$  in one set of experiments and 150-300  $\mu\text{m}$  in the other set. The data for a third set of composites with Ni inclusion size of 100-150  $\mu\text{m}$  have been omitted to maintain clarity. It is seen that both the glass sample and the composite with the Ni inclusion size of 150-300  $\mu\text{m}$  reached nearly full density within approximately the same sintering time. The composite with the Ni inclusion size of 6-10  $\mu\text{m}$ , however, reached a density of  $\sim 0.93$ .

As outlined earlier, the creep of nearly fully dense samples was also studied. Figure 19 shows the axial strain versus time for the dense unreinforced glass samples and composites containing 10 v% inclusions with three different sizes. The applied uniaxial stress was 18 kPa. The strain at any time was smaller for the composite compared to the unreinforced sample and decreased with decreasing inclusion size. Corresponding data for composites containing 20 v% inclusions with two different sizes (150-300 and 6-10  $\mu\text{m}$ ) are shown in Fig. 20. For these composites, the sample with the larger inclusion size was nearly fully dense but that with the lower inclusion size had a matrix density of only  $\sim 0.85$ .

Figure 21 shows the creep viscosity versus the matrix density,  $\rho_m$ , for the unreinforced glass and the glass matrix composites containing 10 v% Ni inclusions. (The units for the viscosity are MPa.min, and not MPa/min as printed on the figures.) Over most of the density range ( $\rho_m$  up to  $\sim 0.90$ ), the viscosity of the composite is insensitive to the presence of the inclusions. Above  $\rho_m \sim 0.90$ , the viscosity shows a small dependence on the inclusion size and this is confirmed by the data for the fully dense samples. The viscosity of the fully dense samples increases by a factor of  $\sim 5$  from the unreinforced glass to the composite with Ni inclusion particles of 6-10  $\mu\text{m}$ .

The creep viscosity as a function of  $\rho_m$  for the composites with 20 v% Ni particles is

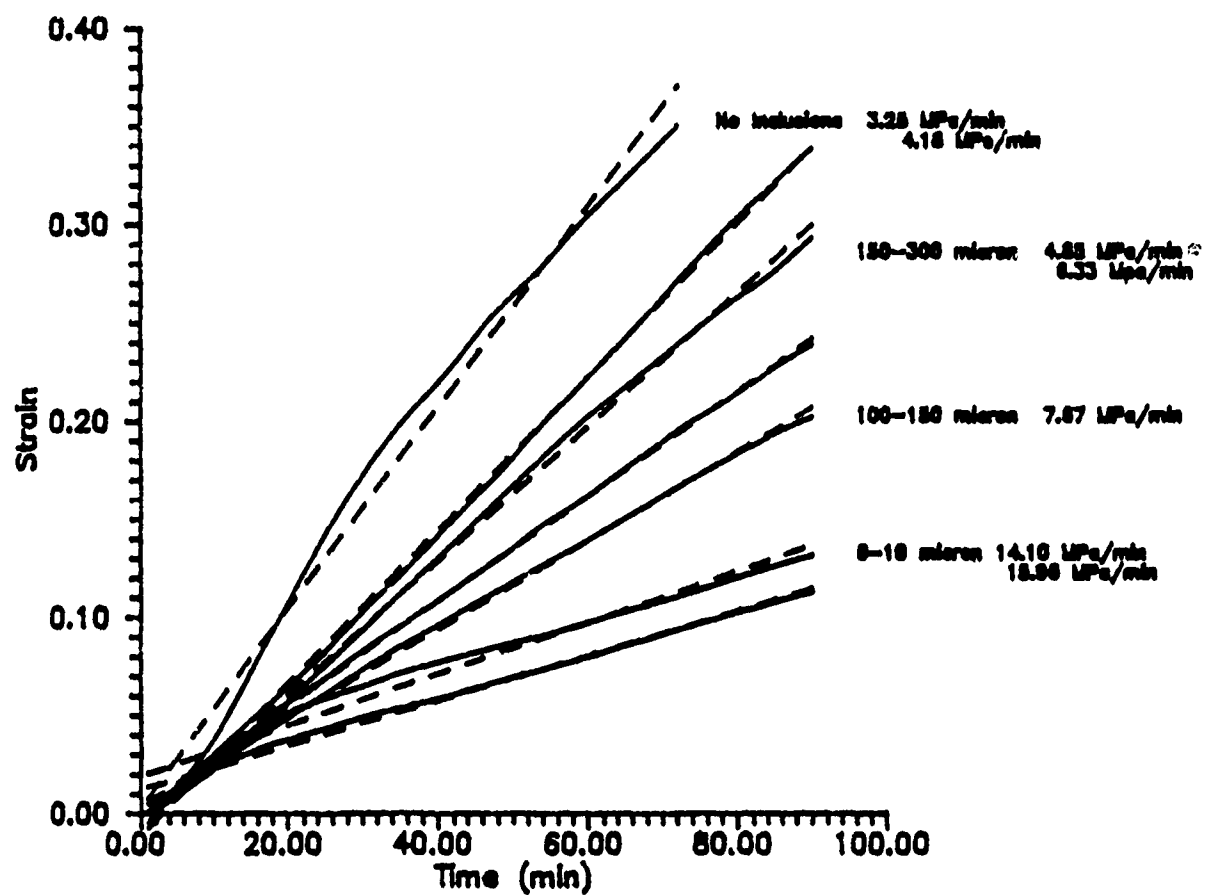


Fig.19 : Axial strain versus time for nearly fully dense samples of glass and glass / 10 V% Ni composite subjected to a uniaxial stress of 18 kPa.

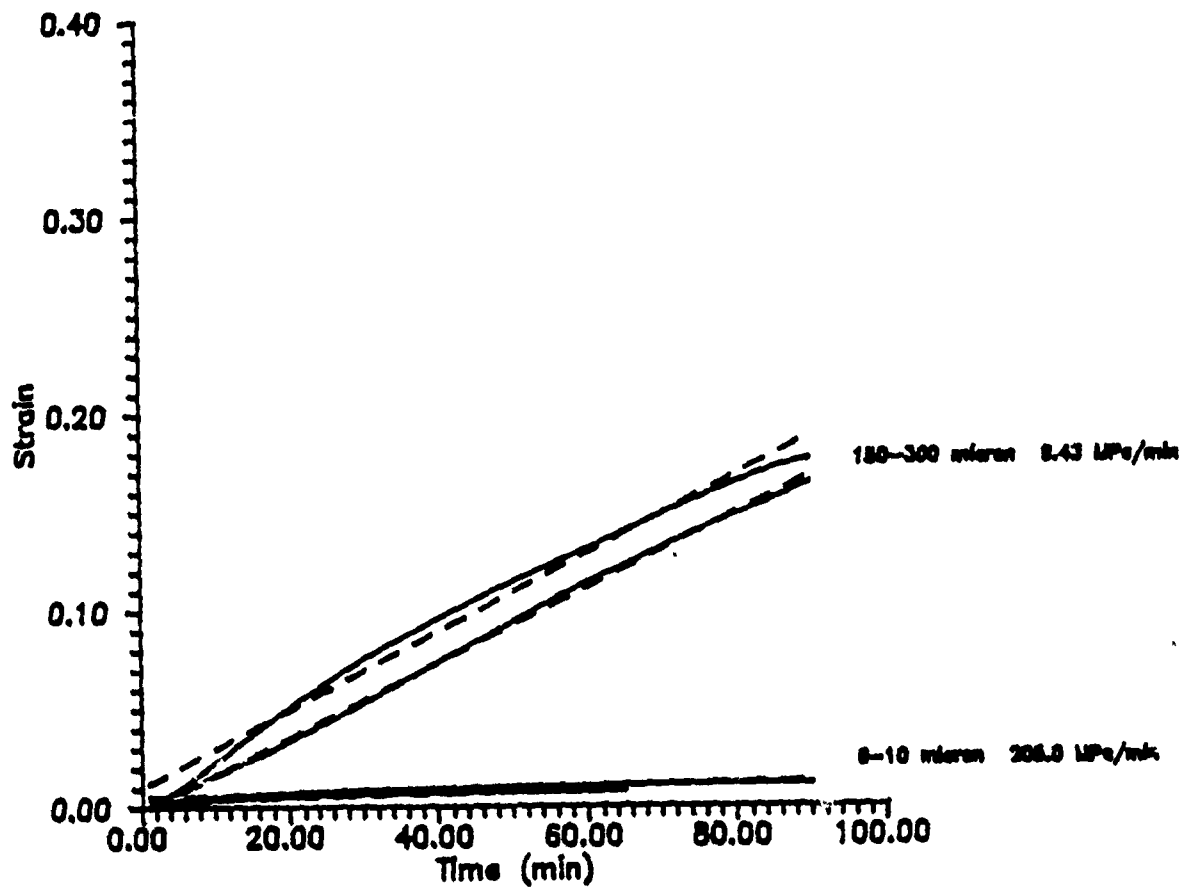


Fig.20 : Axial strain versus time for dense glass / 20 V% Ni composites subjected to a uniaxial stress of 18 kPa.

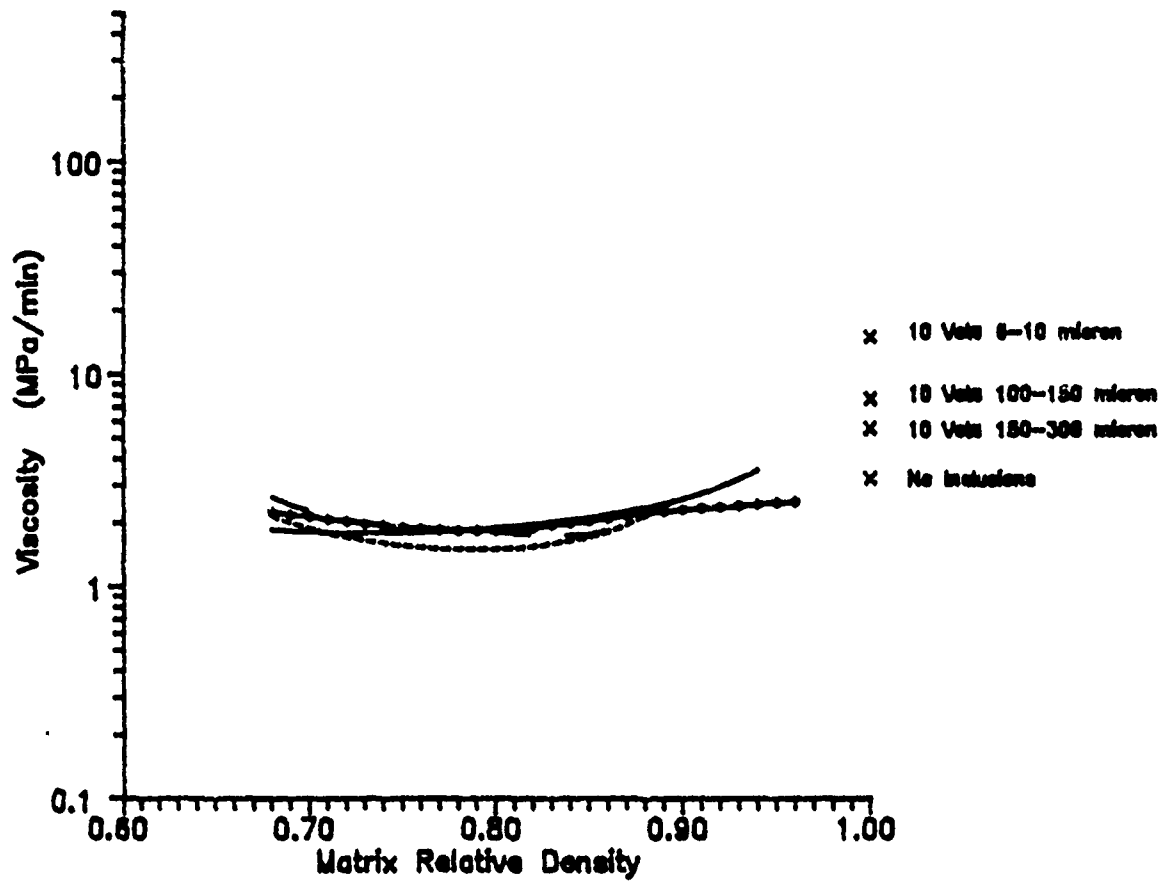


Fig.21 : Creep viscosity versus matrix density for glass and glass / 10 V% Ni composites at 730°C.

shown in Fig. 22. For comparison, the viscosity of the unreinforced glass is also shown. A much stronger inclusion size effect is observed. At a density of  $\sim 0.85$ , the viscosity of the composite with Ni inclusion size of  $6\text{-}10 \mu\text{m}$  is more than 2 orders of magnitude greater than the viscosity of the unreinforced glass.

Scanning electron micrographs of a glass composite containing 10 v% Ni inclusions ( $150\text{-}300 \mu\text{m}$ ) after (a) the pre-sintering step and (b) sintering for 42 min are shown in Fig. 23. The inclusions are well dispersed within the matrix and after sintering, the glass is fully densified around the inclusions. Corresponding micrographs for the composite with inclusions  $6\text{-}10 \mu\text{m}$  in size are shown in Fig. 24. The inclusions are somewhat agglomerated and after sintering, the glass was unable to fill the pores within the agglomerates.

The data show that for the inclusion size of  $6\text{-}10 \mu\text{m}$  (which is comparable to the particle size of the glass powder) the viscosity of the composite increases dramatically in the range of 10-20 v% inclusions. These results are somewhat similar in nature to the theoretical predictions of Scherer and Jagota<sup>18</sup>. They indicate that inclusion particle interactions are responsible for the reduced densification rates above 10 v%. It would be interesting to determine how the viscosity of polycrystalline composites depends on inclusion size and volume fraction.

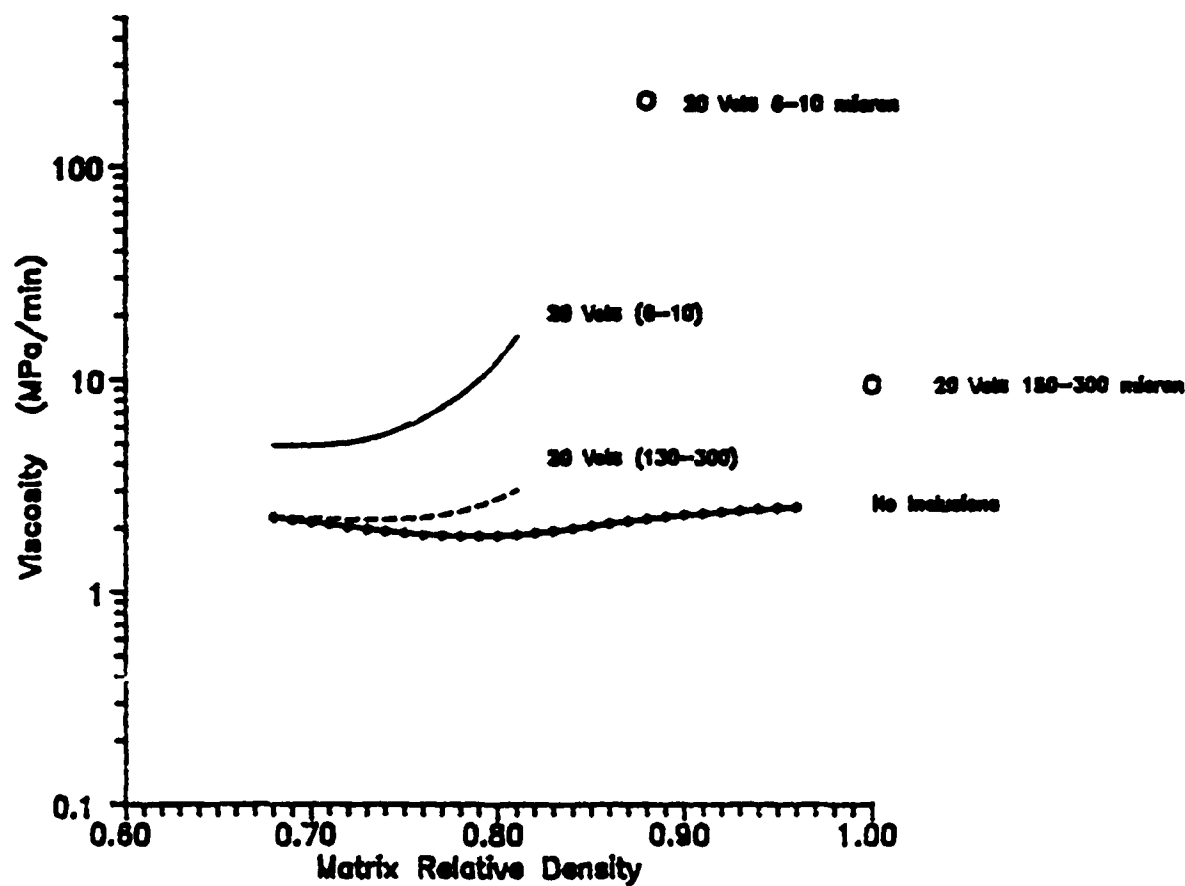
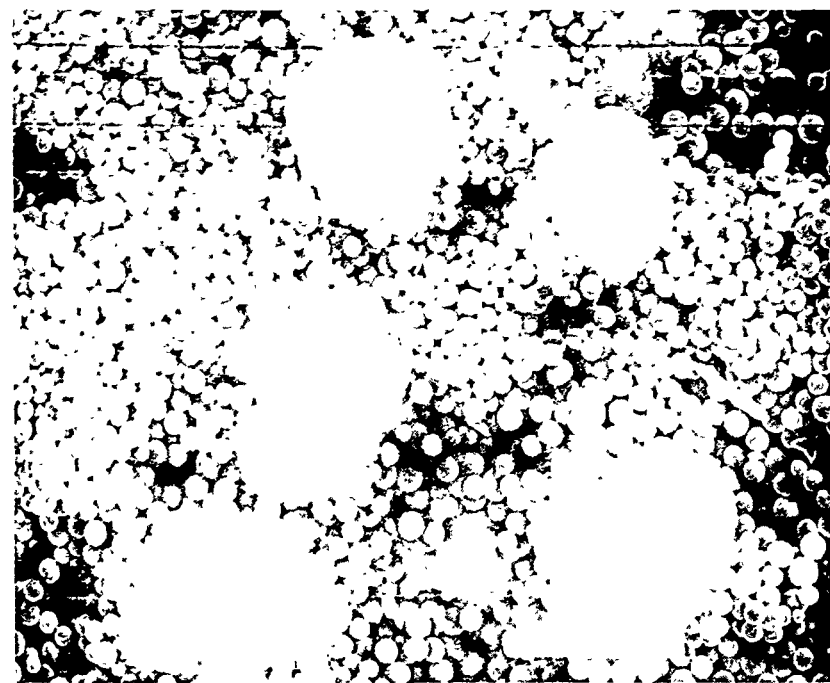
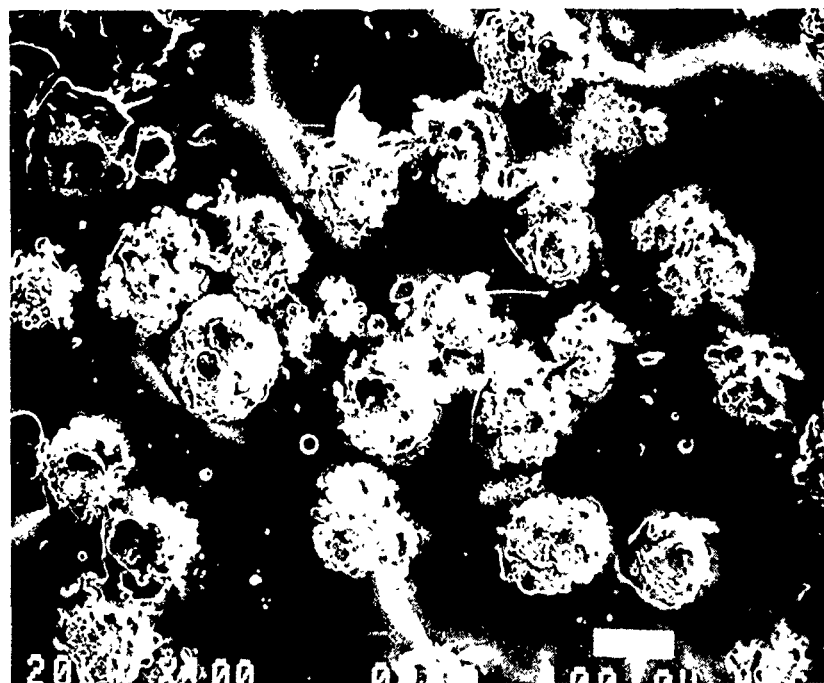


Fig.22 : Creep viscosity versus matrix density for glass an glass / 20 V% Ni composites, compared to the viscosity for the unreinforced glass.

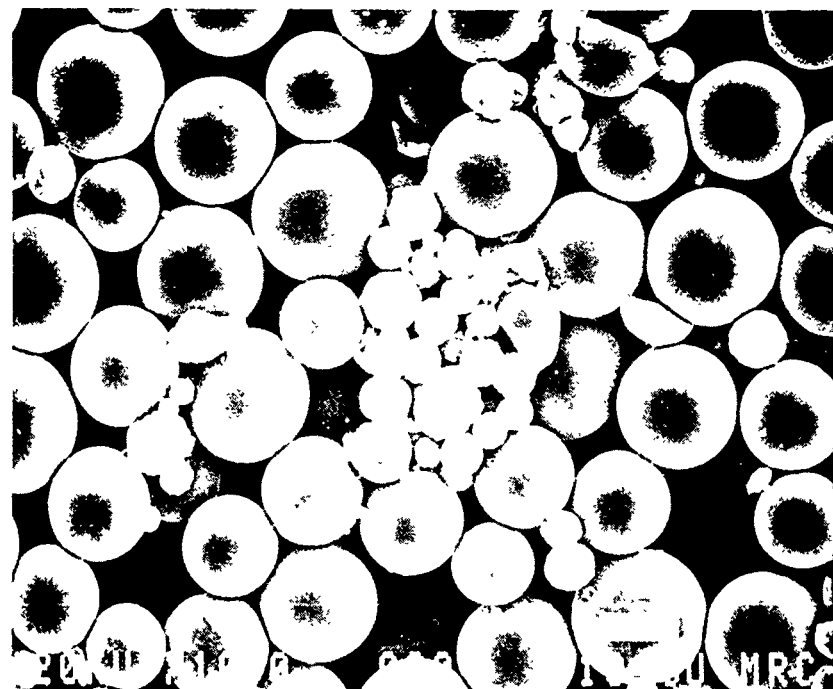


(a)

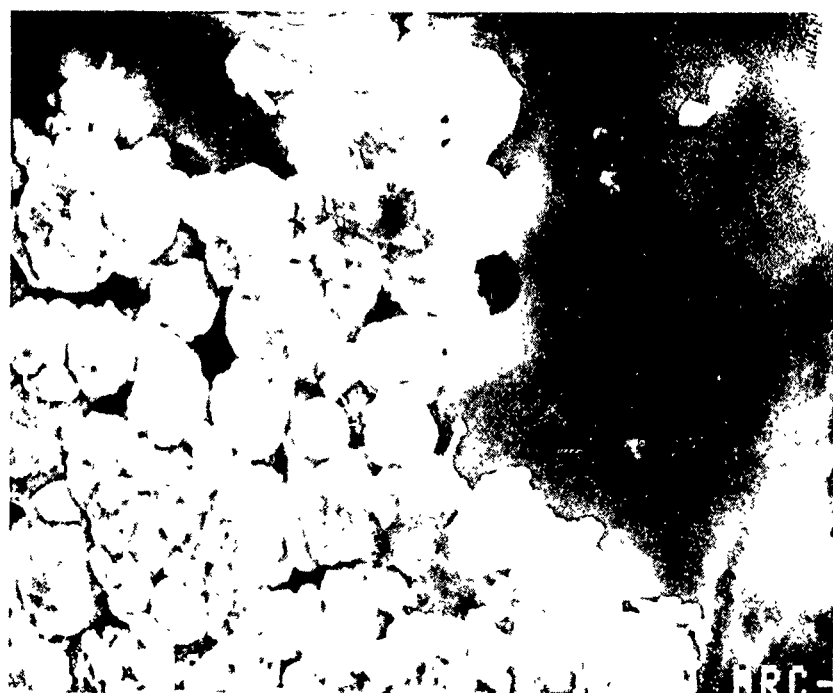


(b)

Fig.23 : Scanning electron micrographs of a glass / 10 V% Ni composite (Ni particle size 150-300 micron) after (a) pre-firing for 20 min at  $710^{\circ}\text{C}$  and (b) after sintering 42 min at  $730^{\circ}\text{C}$ .



(a)



(b)

Fig. 24 : Scanning electron micrographs of a glass / 10 V% Ni composite (Ni particle size 6-10 micron) after (a) pre-firing for 20 min at 710°C and (b) after sintering 42 min at 730°C.

## 2.3 THEORETICAL MODELING

### 2.3.1 Background.

It has been observed that the presence of coarse, inert, rigid inclusions in a fine grained matrix drastically reduces the densification rates in the sintering process [1,3].

A significant theoretical modeling work has been done in trying to explain this phenomena. The reasons have been generally attributed to the development of transient stresses and the sintering matrix is commonly assumed to be viscoelastic. A commonly used model system consists of rigid inclusions and viscoelastic matrix, and viscoelastic backstresses are predicted to cancel part of the sintering stress (sintering potential) so that the matrix densification rate is reduced [6,7]. However, Scherer's theory [5] and De Jonghe and Rahaman's analysis [13] showed that the backstresses were too small to account for the drastic reduction in densification rate.

A number of suggestions have been put forward to account for the drastic reduction in the densification rate. Lange [9] proposed network formation of inclusions. However network formation is not significant at inclusion volume fraction below 15% while experiments showed that the densification rates of polycrystalline composite were drastically reduced even at low inclusion volume fraction (< 15%). Lange [8,21] also attributed reduction in densification rate to damage, e.g. voids, in the matrix produced by nonuniform densification. At present, no detail analysis has been done for the damage formation , development and its effect on the reduction in densification rates.

A number of other factors that may lead to the drastic reduction in densification rates in polycrystalline matrix composites suggested by Scherer and Bordia [11]. These include the competition between densification and coarsening , and the development of anisotropies resulting from the unequal stresses in radial and tangential directions

experienced by the shrinking matrix. Very recently, some efforts have been made in analysing each of these problems by using both analytical and numerical methods. Jagota developed a finite element analysis for neck growth between two viscous spherical particles [28] and also used truss structures in simulating the contacts among ceramic powder particles [25]. A semi-analytical solution of a viscous media between two rigid spheres is given by Andareson [24]. But no single factor has been found to be significant alone.

### 2.3.2 Necessity for developing a finite element program.

The objective of the present research is to try to approach some problems for which the closed form solutions are mathematically untractable. A finite element program is developed to describe the constrained sintering matrix through the entire sintering process. Although the heating schedule for a sintering process can be quite different, isothermal sintering has drawn much attention since temperature effect can be excluded. The special situation of the isothermal sintering problem is that the instantaneous free strain rate, as well as the material properties, can be treated as density dependent. The relation between relative density and time derived from experimental data of unconstrained sintering is used to calculate the sintering strain loads which in turn is used in predicting the reduction in densification rate of constrained sintering matrix as shown in Fig.25. The sintering strain load which can be treated as a kind of sintering potential in equivalence can be expressed in terms of relative density  $\rho$  and its time derivative  $\frac{d\rho}{dt}$  of the unconstrained sintering. That is

$$\dot{\varepsilon}_f = -\frac{1}{3\rho} \frac{d\rho}{dt} \quad (2.3.1)$$

However the density of the constrained sintering matrix during the sintering process is not known apriori. This kind of nonlinear problem has to be approached in an incremental

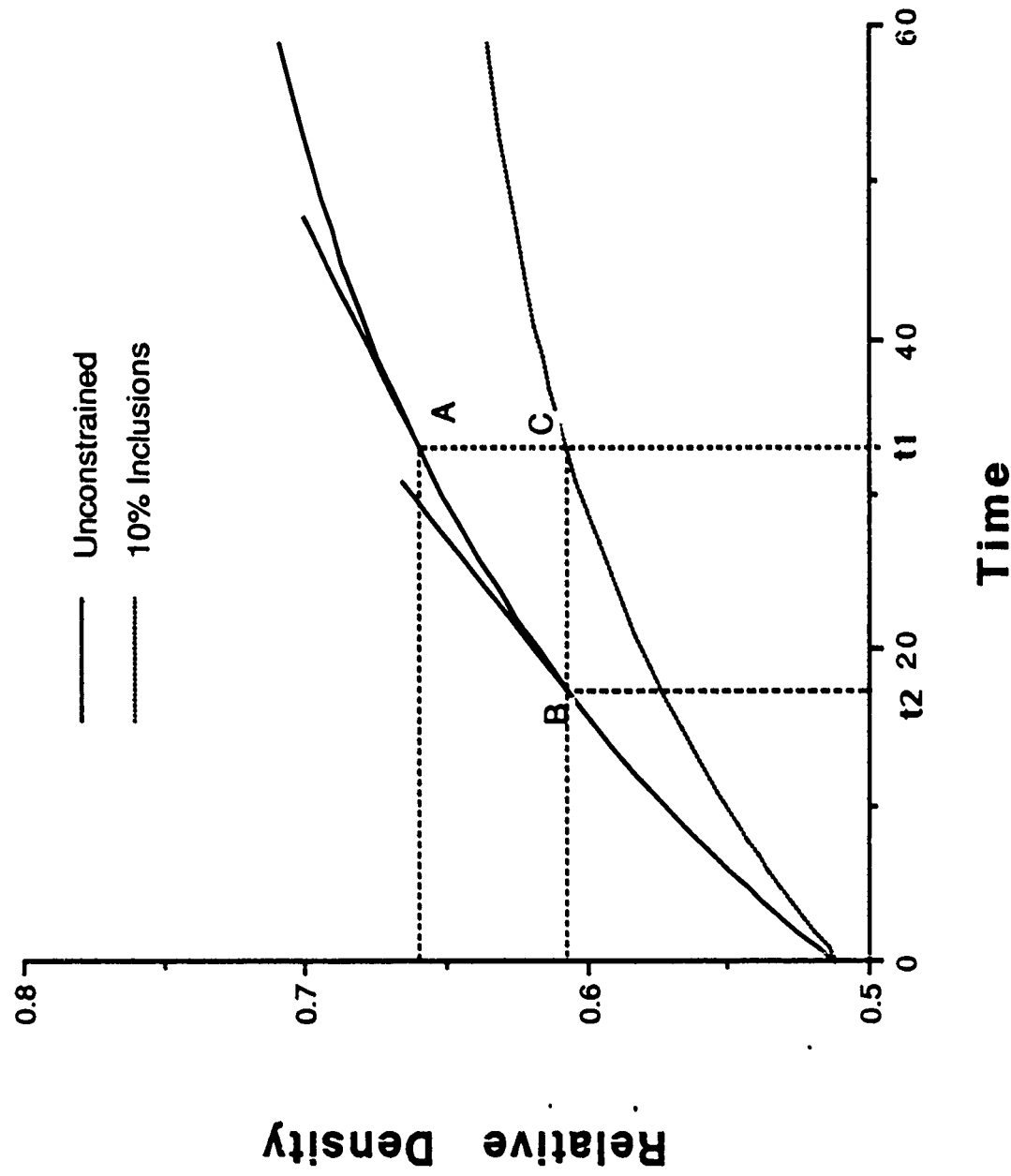


**Fig.25** Experimental data of relative density vs time.

**Fig.25**

fashion. The density calculated from the previous increment is used in determining the instantaneous sintering strain load, as well as the material properties, in the current increment, under the assumption that both the constrained and unconstrained matrices have the same sintering potential at the same density.

Experience with NASTRAN. During the early part this research project, the authors used MSC/NASTRAN program's viscoelastic analysis function in attempting to deal with the sintering problem. NASTRAN is a large finite element analysis package program and has a viscoelastic analysis function. But our experience showed that it is not suitable for simulating the sintering process. The main problem is that the thermal load term which is treated as sintering strain load by taking the thermal coefficient as a linear free strain rate and the temperature variable as time. The incompatibility with the sintering model is that the free strain load can not be linked to density but merely time. Referring to Fig. 25, for example, at time  $t_1$  the relative density of the unconstrained matrix is  $\rho_u$  at point A while the relative density of the constrained matrix is  $\rho_c$  at point C. The slope  $\dot{\rho}$  used in equation (2.3.1) for calculating the free strain load should be the one at point B corresponding to time  $t_2$  not at A corresponding to time  $t_1$ . This shows how the density dependent free strain rate differs from the time dependent one. Since the calculated density from the previous step can not be automatically fed back for use in the next step in NASTRAN, the density dependent sintering strain load can not be satisfied, nor the density dependent material property. These limitations of NASTRAN necessitated the development of a new finite element program for the propose of simulating sintering process.

### 2.3.3 Viscoelastic Formulation.

**General Model.** In viscoelasticity theory, there are two general models [19,32]. The general Maxwell model as shown in Fig.26, consists of multiple simple Maxwell elements in parallel. We consider one of them for studying the sintering behavior. Its total strain rate is

$$\{\dot{\varepsilon}\} = \{\dot{\varepsilon}^e\} + \{\dot{\varepsilon}^v\} + \{\dot{\varepsilon}^s\} \quad (2.3.2)$$

where

- $\{\dot{\varepsilon}\}$  total strain rate
- $\{\dot{\varepsilon}^e\}$  elastic strain rate
- $\{\dot{\varepsilon}^v\}$  viscous strain rate
- $\{\dot{\varepsilon}^s\}$  sintering strain rate

For isotropic viscoelastic material, the viscous component of strain rate  $\{\dot{\varepsilon}^v\}$  can be divided into deviatoric part  $\{\dot{\varepsilon}^d\}$  and volumetric part  $\{\dot{\varepsilon}^k\}$ . As in isotropic elastic case

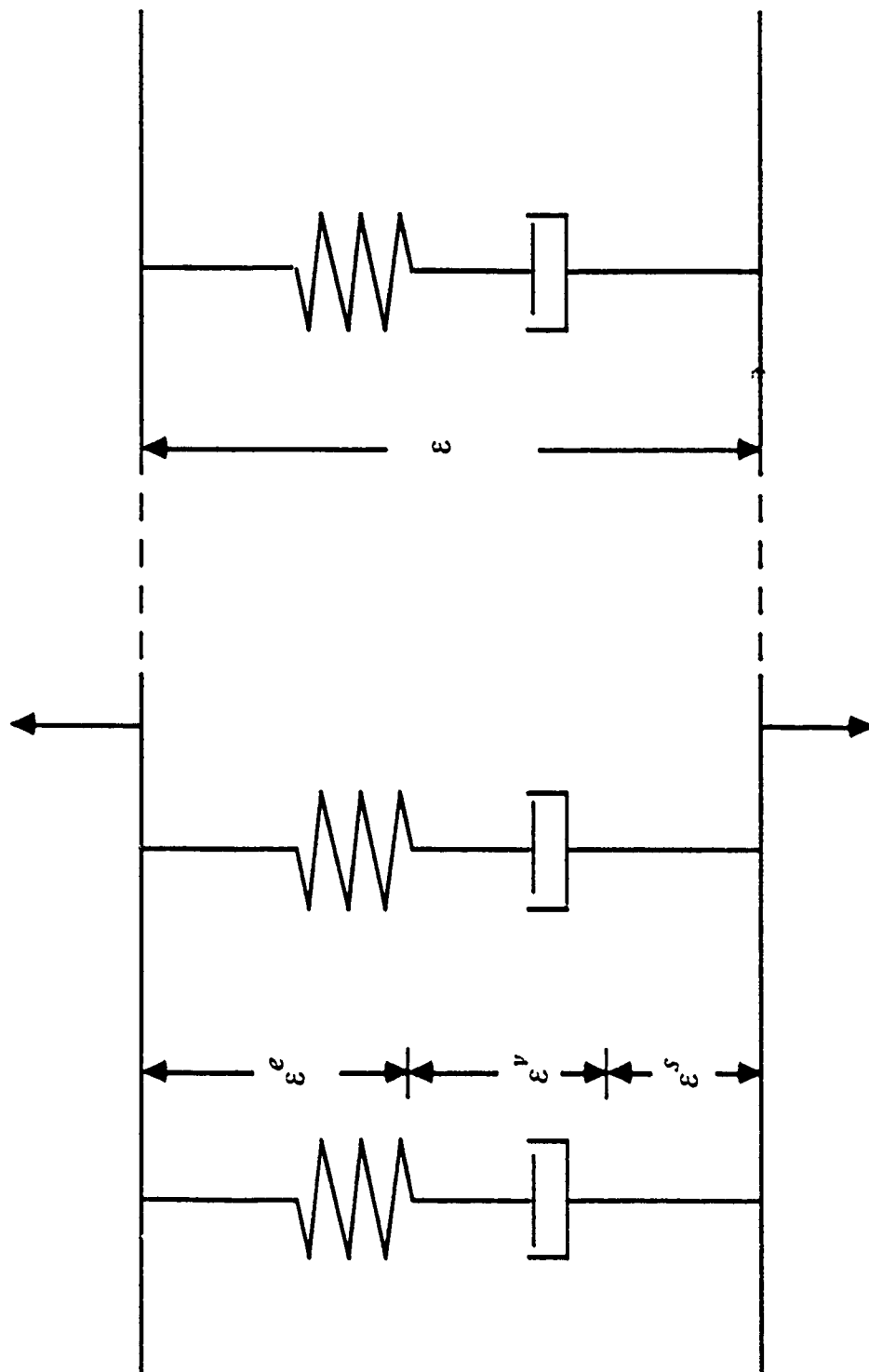
$$\{\dot{\varepsilon}^v\} = \{\dot{\varepsilon}^d\} + \{\dot{\varepsilon}^k\} = \frac{1}{2\eta_\mu} \{\sigma_d\} + \frac{1}{3\eta_K} \{\sigma_m\} \quad (2.3.3)$$

where  $\eta_\mu$  and  $\eta_K$  are shear and bulk viscosities, respectively. So that in 3 dimension, equation (2.3.2) can be expressed as

$$\begin{Bmatrix} \dot{\varepsilon}_x \\ \dot{\varepsilon}_y \\ \dot{\varepsilon}_z \\ \dot{\gamma}_{yz} \\ \dot{\gamma}_{zx} \\ \dot{\gamma}_{xy} \end{Bmatrix} = \begin{Bmatrix} \dot{\varepsilon}_x^e \\ \dot{\varepsilon}_y^e \\ \dot{\varepsilon}_z^e \\ \dot{\gamma}_{yz}^e \\ \dot{\gamma}_{zx}^e \\ \dot{\gamma}_{xy}^e \end{Bmatrix} + \frac{1}{2\eta_\mu} \begin{Bmatrix} \sigma_x^d \\ \sigma_y^d \\ \sigma_z^d \\ 2\tau_{yz} \\ 2\tau_{zx} \\ 2\tau_{xy} \end{Bmatrix} + \frac{1}{3\eta_K} \begin{Bmatrix} \sigma_m \\ \sigma_m \\ \sigma_m \\ 0 \\ 0 \\ 0 \end{Bmatrix} + \begin{Bmatrix} \alpha \\ \alpha \\ \alpha \\ 0 \\ 0 \\ 0 \end{Bmatrix} \quad (2.3.4)$$

where  $\alpha (= -\dot{\rho}/3\rho)$  is linear free strain rate. Let shear and bulk elastic moduli be denoted as  $\mu$  and  $K$  respectively, then shear and bulk relaxation times  $\tau_\mu$  and  $\tau_K$  are defined as:

Fig.26 General Maxwell Model



$$\tau_\mu = \frac{\eta_\mu}{\mu}, \quad \tau_K = \frac{\eta_K}{K} \quad (2.3.5)$$

and the deviatoric and volumetric stresses are

$$\sigma_x^d = (2\sigma_x - \sigma_y - \sigma_z)/3,$$

$$\sigma_y^d = (2\sigma_y - \sigma_z - \sigma_x)/3,$$

$$\sigma_z^d = (2\sigma_z - \sigma_x - \sigma_y)/3,$$

$$\sigma_m = (\sigma_x + \sigma_y + \sigma_z)/3$$

After some matrix manipulation with elastic stiffness matrix, the following relation is obtained

$$\{\dot{\sigma}\} = [D]\{\dot{\varepsilon}\} - 3K\{\dot{\varepsilon}^s\} - \frac{1}{\tau_\mu} \{\sigma^d\} - \frac{1}{\tau_K} \{\sigma_m\} \quad (2.3.6)$$

where  $[D]$  is the elastic stiffness matrices.

For the general Maxwell model consisting of multiple simple Maxwell elements in parallel, the expression becomes a summation over each of these simple Maxwell elements

$$\{\dot{\sigma}\} = \left( \sum_i [D_i] \right) \{\dot{\varepsilon}\} - \sum_i \left( 3K_i \{\dot{\varepsilon}_i^s\} + \frac{1}{\tau_{\mu_i}} \{\sigma_i^d\} + \frac{1}{\tau_{K_i}} \{\sigma_{m_i}\} \right) \quad (2.3.7)$$

Similar expressions for the general Kelvin model, shown in Fig.27, consisting of one simple Maxwell element and multiple simple Kelvin elements in a series can also be obtained. However, for most materials, it is very difficult to obtain parameters for the

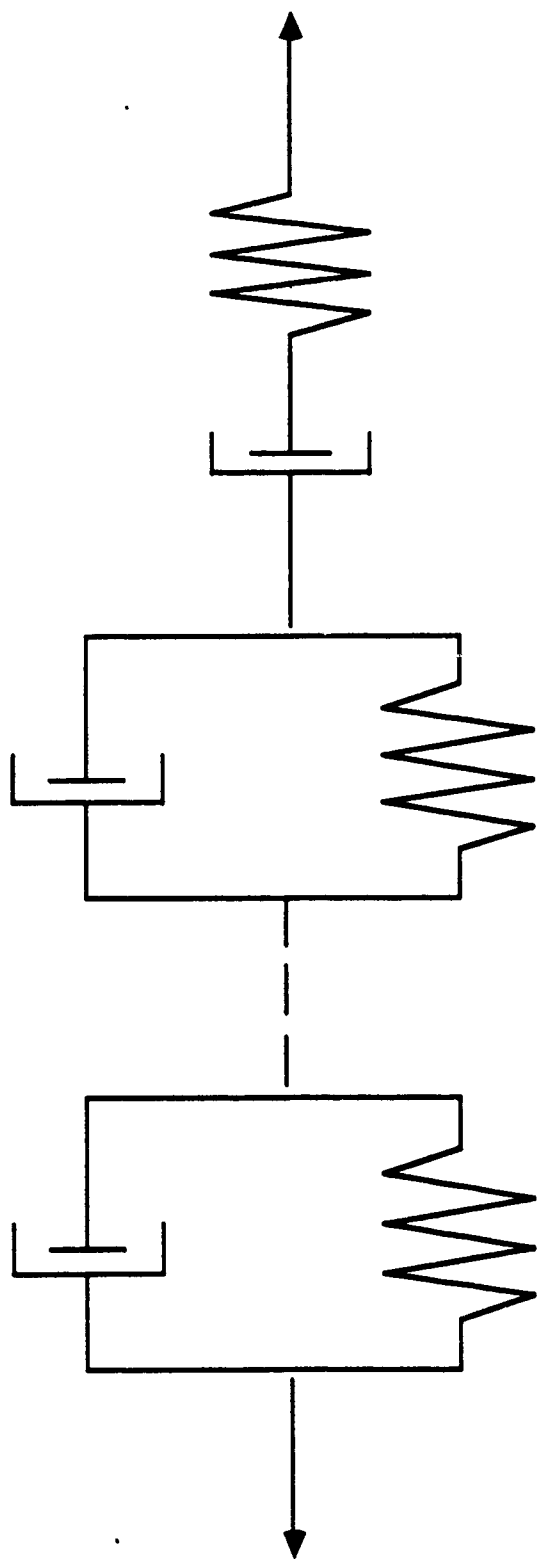


**Fig. 27      General Kelvin Model**

multiple element models. An efficient experimental technique of obtaining the material parameters even in the three or four element standard solid model for ceramics is yet to be developed [30]. It is therefore practical to incorporate only the standard solid model into the finite element formulation as done in several package programs, such as NASTRAN and ADINA.

Standard Solid Model. The standard solid model consists of one simple Maxwell element and one simple Kelvin element as shown in Fig. 28. For a Kelvin element,

$$\{\dot{\sigma}^d\} = 2\mu_2\{\dot{\varepsilon}^d\} + 2\eta_{\mu_2}\{\dot{\varepsilon}^d\}, \quad \{\sigma_m\} = 3K_2\{\varepsilon_m\} + 3\eta_{K_2}\{\dot{\varepsilon}_m\} \quad (2.3.8)$$

hence

$$\{\dot{\varepsilon}^d\} = \frac{1}{2\eta_{\mu_2}}\{\dot{\sigma}^d\} - \frac{1}{\tau_{\mu_2}}\{\varepsilon^d\}, \quad \{\dot{\varepsilon}_m\} = \frac{1}{3\eta_{K_2}}\{\dot{\sigma}_m\} - \frac{1}{\tau_{K_2}}\{\varepsilon_m\} \quad (2.3.9)$$

In the standard solid model,

$$\{\dot{\varepsilon}^d\} = \frac{1}{2\mu}\{\dot{\sigma}^d\} + \left( \frac{1}{2\eta_\mu} + \frac{1}{2\eta_{\mu_2}} \right)\{\dot{\sigma}^d\} - \frac{1}{\tau_{\mu_2}}\{\varepsilon^d\} \quad (2.3.10)$$

$$\{\dot{\varepsilon}_m\} = \frac{1}{3K_2}\{\dot{\sigma}_m\} + \left( \frac{1}{3\eta_K} + \frac{1}{3\eta_{K_2}} \right)\{\dot{\sigma}_m\} - \frac{1}{\tau_{K_2}}\{\varepsilon_m\} \quad (2.3.11)$$

$$\{\dot{\sigma}^d\} = 2\mu\{\dot{\varepsilon}^d\} - \mu\left( \frac{1}{\eta_\mu} + \frac{1}{\eta_{\mu_2}} \right)\{\dot{\sigma}^d\} + 2\mu\left( \frac{1}{\tau_{\mu_2}}\{\varepsilon^d\} \right) \quad (2.3.12)$$

$$\{\dot{\sigma}_m\} = 3K\{\dot{\varepsilon}_m\} - K\left( \frac{1}{\eta_K} + \frac{1}{\eta_{K_2}} \right)\{\dot{\sigma}_m\} + 3K\left( \frac{1}{\tau_{K_2}}\{\varepsilon_m\} \right) + 3K\{\dot{\varepsilon}_m\} \quad (2.3.13)$$

simpler models can be obtained by setting any of  $\mu$ ,  $K$ ,  $\eta_\mu$ ,  $\eta_K$ ,  $\mu_2$ ,  $K_2$ ,  $\eta_{\mu_2}$  and  $\eta_{K_2}$  to be either infinity or zero.

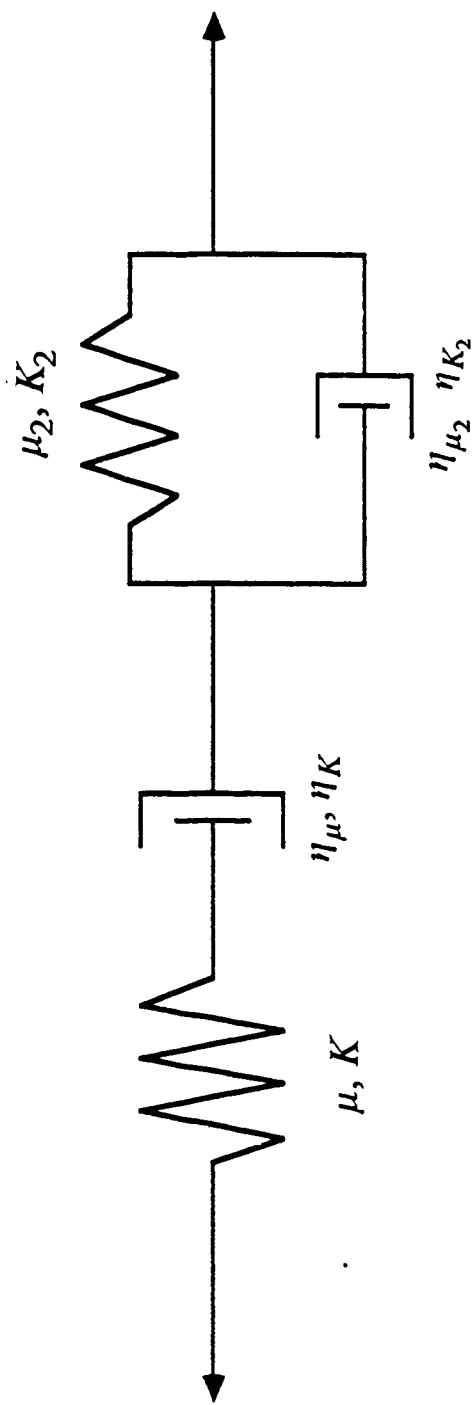


Fig. 28. Standard Solid Model

### 2.3.4 Finite Element Program.

This computer code is used for viscoelastic analysis of the sintering matrix with inclusions by the finite element method. A brief description of a simple Maxwell model in two dimension (plane strain) is given below.

Solution Procedure. At the beginning of  $n$ th time step , the volume around each sampling point (usually Gaussian's point) is calculated by the Gaussian's numerical integration

$$V_s^n = J(\xi, \zeta) w_\xi w_\zeta \quad (2.3.14)$$

where the  $J(\xi, \zeta)$  is the Jacobian's matrix mapping the element from the global coordinates to the local coordinates, the  $w_\xi$  and  $w_\zeta$  are the weight coefficients at the sampling point in local coordinates  $(\xi, \zeta)$  .

Then the relative density averaged over that sampling volume can be calculated as

$$\rho^n = \frac{\rho^0 V_s^0}{V_s^n} \quad (2.3.15)$$

The linear free strain rate is calculated as

$$\dot{\varepsilon}_f = - \frac{1}{3\rho} \frac{d\rho_u(\rho)}{dt} \quad (2.3.16)$$

where  $\rho_u$  is the relative density of the unconstrained matrix.

The constitutive parameters are all density dependent,

$$E^n = E(\rho^n) \quad (2.3.17)$$

$$v^n = v(\rho^n) \quad (2.3.18)$$

$$\eta^n = \eta(\rho^n) \quad (2.3.19)$$

then the shear modulus and relaxation time can be derived as

$$\mu^n = \frac{E^n}{2(1 + v^n)} \quad (2.3.20)$$

$$\tau^n = \frac{\eta^n}{\mu^n} \quad (2.3.21)$$

The current coordinates of nodes are

$$\{x^n\} = \{x^{n-1}\} + \{\Delta u^{n-1}\} \quad (2.3.22)$$

The current strain-displacement relation matrix is

$$[B^n] = [B(\{x^n\})] \quad (2.3.23)$$

The current elastic stress-strain relation matrix is

$$[D^n] = [D(\mu^n, v^n)] \quad (2.3.24)$$

For convenience, a coefficient of the simple Maxwell model is denoted as

$$k^n = \frac{1}{1 + \frac{\Delta t^n}{2\tau^n}} \quad (2.3.25)$$

The equation of equilibrium [29] is

$$\int_{\Omega} [B^n]^T \{\sigma^n\} d\Omega + f^n = 0 \quad (2.3.26)$$

The incremental form of equilibrium equation is

$$\int_{\Omega} [B^n]^T \{\Delta\sigma^n\} d\Omega + \Delta f^n = 0 \quad (2.3.27)$$

The viscoelastic stress-strain relation of simple Maxwell model in plane strain is

$$\{\Delta\sigma^n\} = k^n [D^n] ([B^n] \{\Delta u^n\} - (1 + v^n) \{\Delta \varepsilon_f^n\}) - (\frac{\Delta t^n}{\tau^n}) k^n \{\sigma^n\} \quad (2.3.28)$$

where

$$\{\sigma^n\} = \{\sigma^{n-1}\} + \{\Delta\sigma^{n-1}\} \quad (2.3.29)$$

Substituting the  $\{\Delta\sigma^n\}$  into the incremental form of equilibrium equation (2.3.27) yields

$$\begin{aligned} \left( k^n \int_{\Omega} [B^n]^T [D^n] [B^n] d\Omega \right) \{\Delta u^n\} &= k^n (1 + v^n) \int_{\Omega} [B^n]^T [D^n] \{\Delta \varepsilon_f^n\} d\Omega \\ &+ k^n (\frac{\Delta t^n}{\tau^n}) \int_{\Omega} [B^n]^T \{\sigma^n\} d\Omega - \Delta f^n + \Phi^n \end{aligned} \quad (2.3.30)$$

where  $\Phi^n$  is called the residual force

$$\Phi^n = \int_{\Omega} [B^n]^T \{\sigma^n\} d\Omega + f^n \neq 0 \quad (2.3.31)$$

because the error from each increment makes the equation of equilibrium not exactly satisfied, adding the residual force to the next time step can not only reduce the error but also reduce iterations [27]. Finally the simultaneous equations are in the form as

$$\left( k^n \int_{\Omega} [B^n]^T [D^n] [B^n] d\Omega \right) \{ \Delta u^n \}$$

$$= \int_{\Omega} [B^n]^T \left[ k^n (1 + v^n) [D^n] \{ \Delta \varepsilon_f^n \} + (k^n \frac{\Delta t^n}{\tau^n} + 1) \{ \sigma^n \} \right] d\Omega + f^{n-1} \quad (2.3.32)$$

Simply

$$[K_T^n] \{ \Delta u^n \} = \{ \Delta F^n \} \quad (2.3.33)$$

where  $[K_T]$  is termed as the tangential stiffness matrix,

$$[K_T^n] = k^n \int_{\Omega} [B^n]^T [D^n] [B^n] d\Omega \quad (2.3.34)$$

the  $\{ \Delta F^n \}$  is called pseudo force,

$$\{ \Delta F^n \} = \int_{\Omega} [B^n]^T [k^n (1 + v^n) [D^n] \{ \Delta \varepsilon_f^n \} + (k^n \frac{\Delta t^n}{\tau^n} + 1) \{ \sigma^n \}] d\Omega + f^{n-1} \quad (2.3.35)$$

By assembling the simultaneous equations, applying the boundary condition and solving, we get  $\{ \Delta u^n \}$  and then calculate the new coordinates

$$\{ x^{n+1} \} = \{ x^n \} + \{ \Delta u^n \} \quad (2.3.36)$$

new  $[B^*]$  is then modified by using  $\{x^{n+1}\} = \{x^n\} + \{\Delta u^n\}$  to form new stiffness matrix for iterations. After error between two iterations becomes smaller than a critical value for convergence, the same routine is repeated for the  $(n + 1)th$  time step.

Solution Technique. There are several methods for solving nonlinear simultaneous equations [27] in general, but no one is perfect for every problem. In order to get the correct result, the intervals of time steps should be sufficiently small and iterations large enough for getting a convergent and stable solution at that step. On the other hand, increment lengths are sought to be large and iterations to be fairly few to reduce the computer time. The strategy of balancing the increment intervals and iterations is a matter of experience. A combination of Euler's rule [27] and residual force correction [29] is used in this code to reduce iterations on each step. And the assumption that the stress varies linearly during each time step is used so that the increments can be taken relatively larger. The procedures for reducing iterations and increasing the allowable increment lengths have made this code fairly efficient so that we can simulate a longer sintering process

Free strain rate and Constitutive Parameters. The sintering strain loads are derived from experiments made by Rahaman [1] and some of his unpublished data. In the process of isothermal sintering, the temperature is quickly increased to and then is kept constant at 750 °C. The relative density of the unreinforced matrix  $\rho_u$  is measured versus time. The sintering matrix is considered to be viscoelastic. Maxwell model was used to simulate the behavior of the matrix under stresses. The viscosity coefficient  $\eta$  is measured by the technique of loading dilatometry [15]. The Young's modulus  $E$  and Poisson's ratio are assumed [23].

Features compared with NASTRAN. This computer code not only has some viscoelastic (creep) analysis functions similar to that NASTRAN does, but also has some special functions for the sintering problem that NASTRAN does not have.

The following are the major differences of this code from NASTRAN:

In this code, the Young's modulus  $E$ , Poisson's ratio  $\nu$  and viscosity  $\eta$  can be made to depend on local density (not only overall density) while in NASTRAN these parameters can only be made to depend on time (or temperature) and should be prescribed apriori. Further, coefficient of viscosity  $\eta$  can only be made stress dependent in NASTRAN.

Coefficient of viscosity specifications can be made as many as needed up to the total number of elements while in NASTRAN all elements must have the same  $\eta$ . This makes it impossible to use NASTRAN, for example, with the three region composite sphere model (see Appendix).

This code can be run on supercomputers, such as CNSF at Cornell, New York and NSCA at Champaign, Illinois, to simulate the entire process of sintering. However NASTRAN as a commercial package program is currently not supported by some of these supercomputers. Nevertheless, this computer code is a base into which new functions can be easily implemented.

### 2.3.5 Preliminary Results and Discussion.

This finite element program has just been developed and is still being tested and undergoing improvements, only a few of simple cases have been studied and the results for these cases are presented.

Single Inclusion Case. A simple mesh was used in single inclusion case (10% volume fraction) as shown in Fig. 29. The average relative density of the constrained matrix against the unconstrained matrix was calculated and compared with the experimental data as shown in Fig. 30. The result reconfirms Scherer's theory as mentioned earlier.

Multiple Inclusion Case. The multiple inclusion model seems more realistic than single inclusion model inspite of idealization of uniform size and distribution of inclusions in the matrix. Due to symmetry, only the shaded region is considered as shown in Fig. 31. A rough element mesh is used as shown in Fig. 32. A rigid element (its Young's modulus is relatively much larger than the rest) is located away from the first inclusion at the origin. The size of the inclusions and distance between them are arranged to match the inclusion volume fraction and 8-noded isoparametric elements are used. The difference in the predicted relative densities for the two cases, single and multiple inclusions, is very minimal, as shown in Fig. 33. This is probably because the region considered was too small and mesh too coarse.

A interesting phenomenon from 'he preliminary' result is that the variation of density is not sensitive to the viscosity coefficient but quiet so to the poisson's ratio. It agrees with results from the viscoelastic analysis (see Appendix) that no volumetric strain except elastic part exsits if the poisson's ratio is constant throughout the process.

Future Work. Since this computer code of finite element analysis has just been set up, it needs to be tested further against available closed form solutions and physical interpretation of the results to ensure the validity of the analyses. This computer code will then be used in analysing and investigating the following problems: The interactions among inclusions; the crack-like damages including pre-existing cracks from cold

compaction and cracks induced while sintering and the effect of matrix damages on the densification rates. In addition, a major effort will be launched to combine non-mechanical factors, such as mass diffusions, grain surface energy minimization and grain growth. Although most of the work will be done by two dimensional simulations, some special problems will be analysed in three dimension to estimate the errors produced by two dimensional approximation.

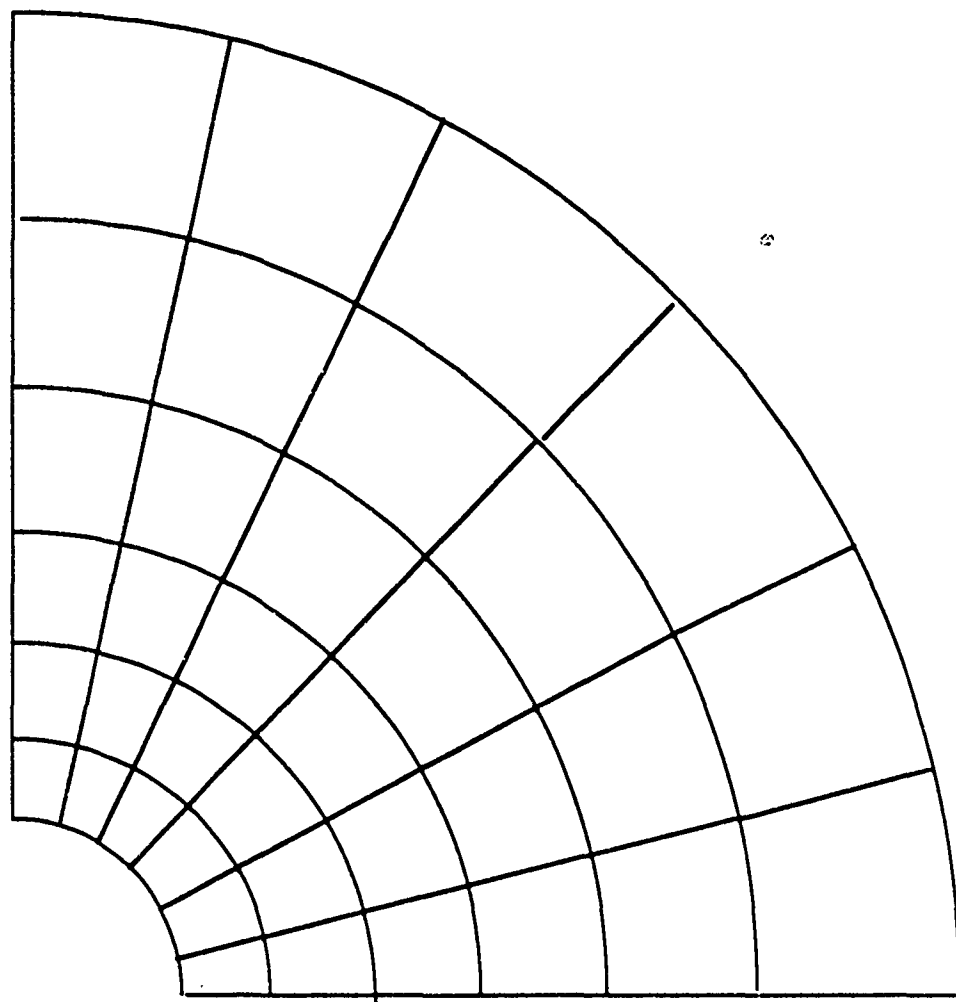


Fig. 29. A simple Finite Element Mesh

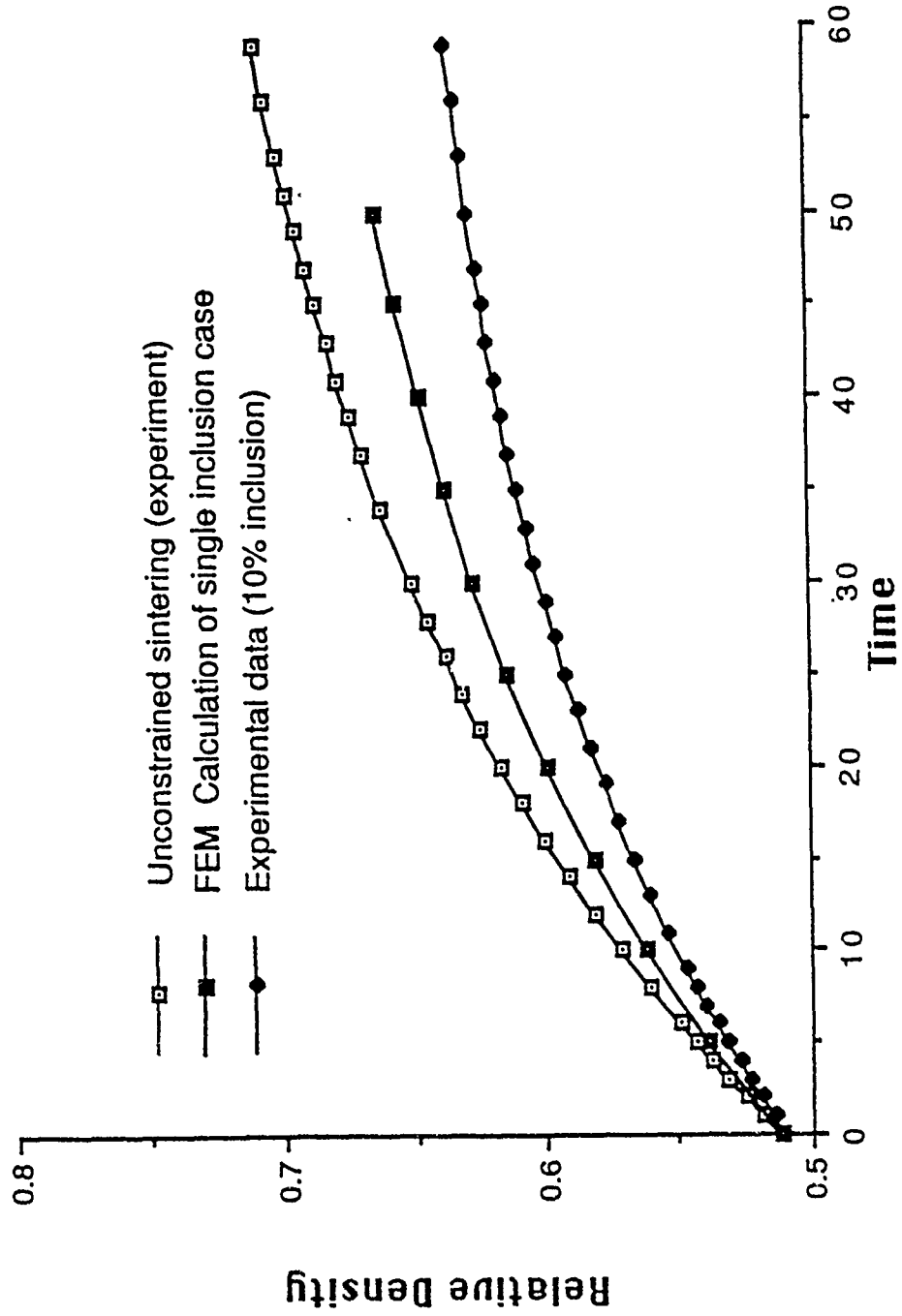
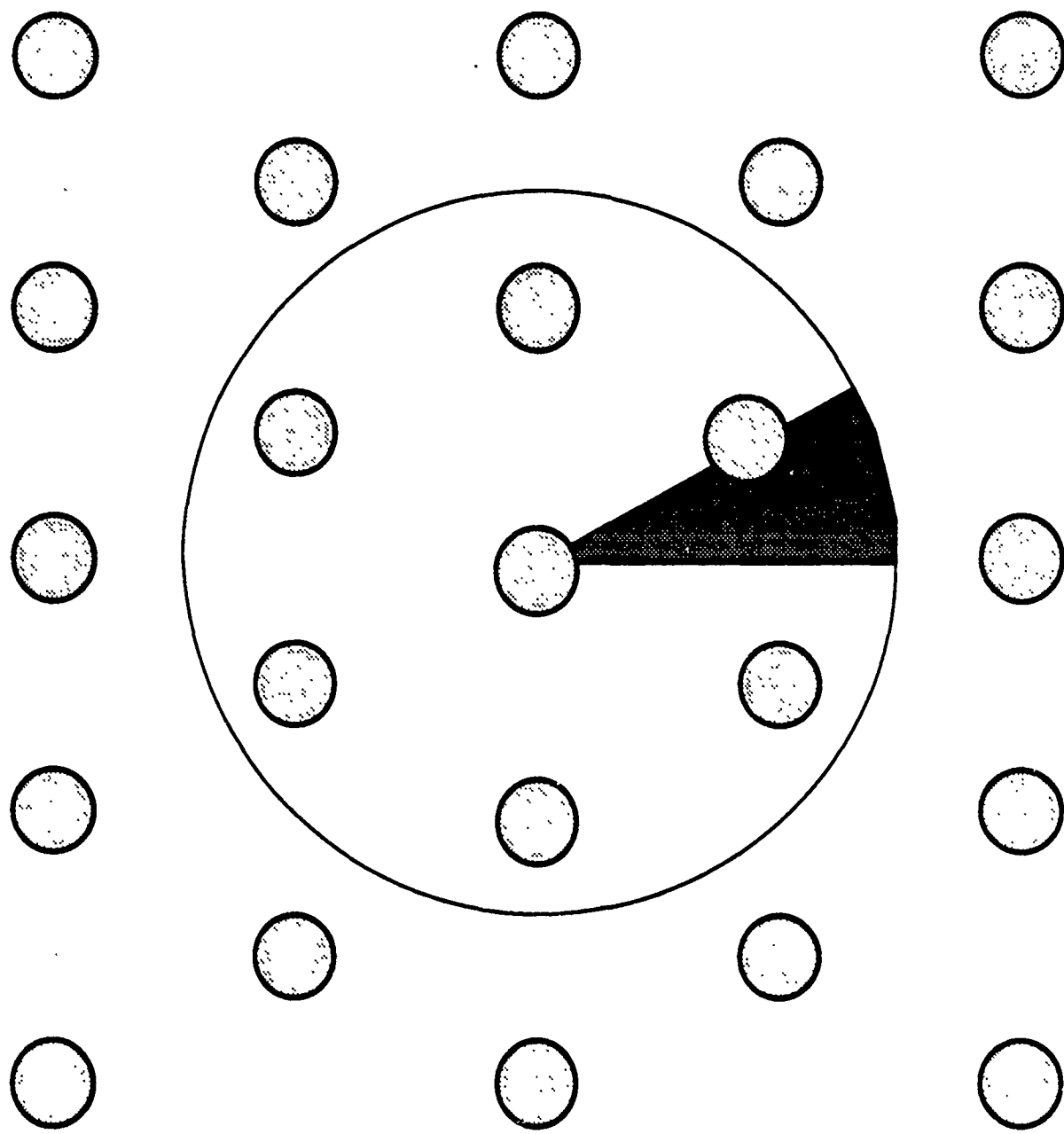


Fig.30 Prediction of the relative density by Finite Element Method.



**Fig.31. Multiple inclusion case is considered by symmetric arrangement of inclusions**

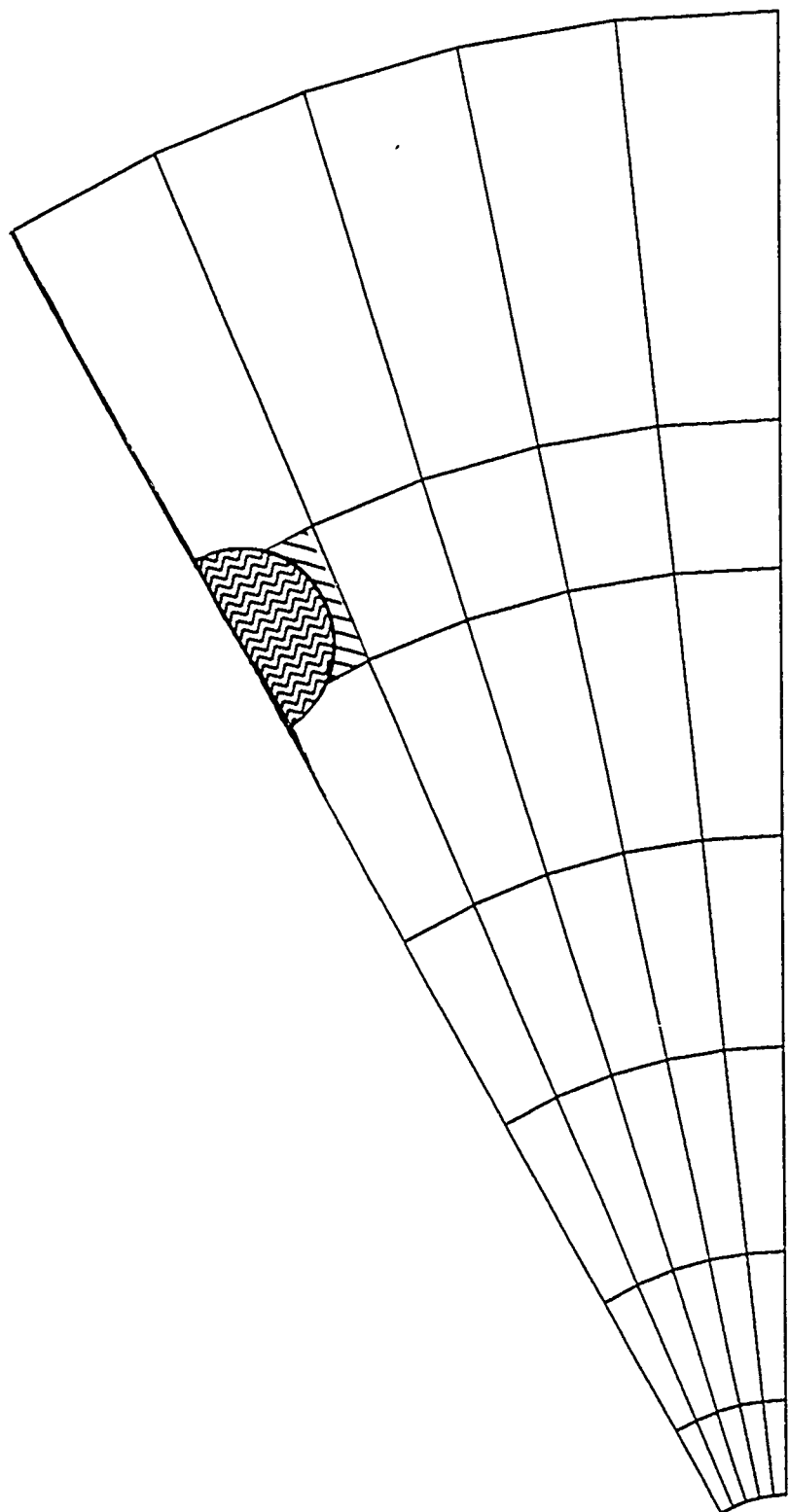


Fig. 32. A Simple Finite Element Mesh of Multiple Inclusion Model

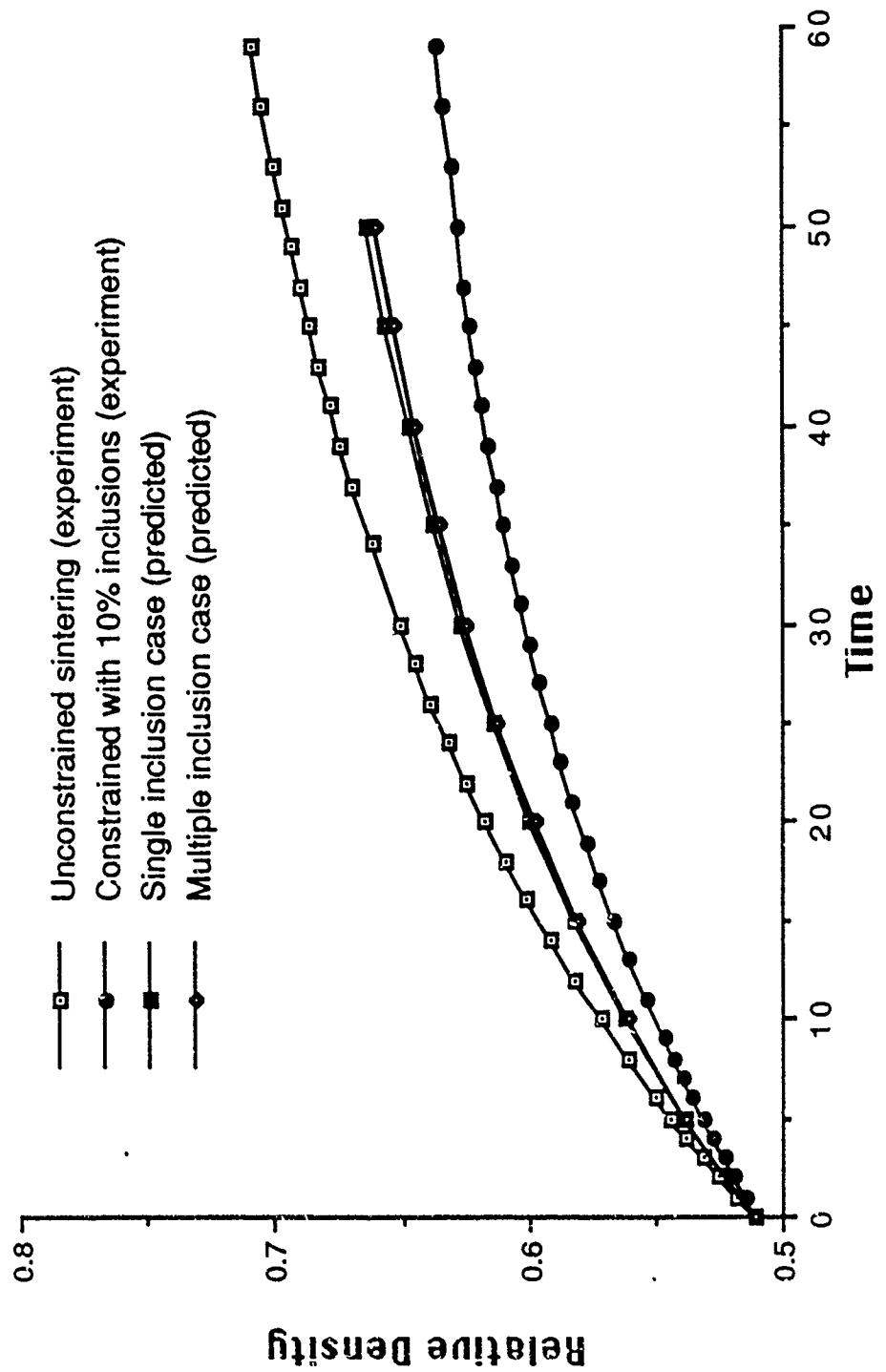


Fig. 33 Predictions for matrix with 10% volume fraction inclusions.

## 2.4 SUMMARY OF ACCOMPLISHMENTS

Experimentally, the effect of key material and processing parameters (e.g. inclusion volume fraction, inclusion size, inclusion distribution, matrix uniformity and sintering temperature) on the sintering of a model polycrystalline ceramic composite has been determined. The composite consisted of a fine-grained ZnO matrix and an inert, rigid, particulate inclusion phase of ZrO<sub>2</sub>.

The sintering behavior of the composite was shown to depend significantly on the method used to form the green composite body.

It was demonstrated that ceramic particulate composites with an appreciable inclusion content can be sintered conventionally to nearly full density if forming methods which minimize inclusion particle interactions and maximize the matrix powder packing immediately surrounding the inclusions were used. As an example, composites containing up to 35 v% inclusions that were formed by coating the inclusion particles with the matrix phase by chemical precipitation followed by die-pressing were sintered to nearly full density under identical sintering conditions used for the unreinforced matrix.

Improved sintering conditions for ceramic composites were shown to prevail at higher temperatures.

For composites formed by conventional processing (i.e. conventional mixing and die-pressing), the densification rate decreased drastically with increasing inclusion volume fraction or with decreasing inclusion size and increased with increasing temperature.

Composites formed by slip casting showed somewhat similar sintering behavior to that for conventionally processed composites.

The main factors controlling the sintering of conventionally processed composites and slip cast composites were shown to involve the packing of the matrix immediately

surrounding the inclusions and inclusion particle interactions that constrained the matrix.

The effect of the inclusion phase on the composite viscosity was determined for a system consisting of a soda-lime glass matrix containing spherical nickel inclusions. For 10 v% inclusions, the composite viscosity was approximately the same as the unreinforced glass and there was almost no effect of the inclusion size. For 20 v% inclusions, the composite viscosity increased significantly with decrease in the inclusion size. The results indicate that interaction between the inclusion particles is an important factor for glass matrix composites containing more than  $\approx$  10 v% inclusions.

Theoretically, modelling studies were initiated to account for the experimental data. A finite element program was developed to describe the data over the entire sintering process. The sintering problem was considered as a special thermomechanical problem in which the instantaneous free strain rate as well as the material properties are density dependent. The effects of single inclusion and multiple inclusion cases and inhomogeneity in the matrix density was determined.

## 2.5 FUTURE WORK

The experiments performed in the first year yielded a number of important results. It is important to determine whether the results are specific to the ZnO/ZrO<sub>2</sub> system studied. The experiment can therefore be extended to a composite system consisting of a fine-grained Al<sub>2</sub>O<sub>3</sub> matrix reinforced with ZrO<sub>2</sub> inclusions.

The experiments will be extended to include whisker reinforced composites. A system consisting of a fine-grained Al<sub>2</sub>O<sub>3</sub> matrix reinforced with SiC whiskers will be utilized.

It is important to determine whether the effect of an inclusion phase on the viscosity of a glass matrix is qualitatively different from that for a polycrystalline matrix. The first-year experiments for glass matrix composites will therefore be extended to a polycrystalline matrix (ZnO) containing ZrO<sub>2</sub> inclusions.

Theoretically, the computer code for the finite element analysis that was developed in the first year will be tested further against available closed form solutions and the validity of the results will be checked. The computer code will then be used to analyze the effects of multiple inclusions, inclusion interactions, and crack-like damage arising from compaction and sintering on the composite densification rate. The incorporation of diffusion-controlled mechanisms for densification and grain growth into the model will also be investigated.

## 2.6 REFERENCES

1. L. C. De Jonghe, M. N. Rahaman, and C. H. Hsueh, "Transient stresses in Bimodal Compacts During sintering", *Acta metall.*, 34 (7) 1467-1471 (1986).
2. R. K. Bordia and R. Raj, "Sintering of  $TiO_2 - Al_2O_3$  Composites: A model Experimental Investigation", *J. Am. Ceram. Soc.*, 71 (4) 302-310 (1988).
3. W. H. Tuan, E. Gilbart, and R. J. Brook, "Sintering of Heterogeneous Ceramic Compacts, Part I:  $Al_2O_3 - Al_2O_3$ ", *J. Mater. Sci.*, 24 1062-1068 (1989).
4. M. N. Rahaman and L. C. De Jonghe, "Effect of Rigid Inclusions on the Sintering of Glass Powder Compacts", *J. Am. Ceram. Soc.*, 70 (12) c-308-c351 (1987).
5. G. W. Scherer, "Sintering with Rigid Inclusions", *J. Am. Ceram. Soc.*, 70 (10) 719-725 (1987).
6. R. Raj and R. K. Bordia, "Sintering of Bimodal Powder Compacts", *Acta Metall.*, 32 (7) 1003-1019 (1984).
7. C. H. Hsueh, A. G. Evans, R. M. Cannon, and R. J. Brook, "Viscoelastic Stresses and Sintering Damage in Heterogeneous Powder Compacts", *Acta Metall.*, 34 (5) 927-936 (1986).
8. F. F. Lange, "Densification of Powder Rings Constrained by Dense Cylindrical Cores", *Acta Metall.*, 37 (2) 697-704 (1989).
9. F. F. Lange, "Constrained Network Model for Predicting Densification Behavior of Composite Powders", *J. Mater. Res.*, 2 (1) 59-65 (1987).

10. M. W. Weiser and L. C. De Jonghe, "Inclusion Size and Sintering of Composite Powders", *J. Am. Ceram. Soc.*, 71 (3) C-125-127 (1988).
11. L. C. De Jonghe and M. N. Rahaman, "Densification of Particulate Ceramic Composites: The Role of Heterogeneities", pp. 353-361 in Mater. Res. Soc Symp. Proc., Vol 155: Processing of Advanced Ceramics Edited by I. A. Aksay. The Materials Research Society, Pittsburg, PA (1989).
12. R. K. Bordia, and G. W. Scherer, "On Constrained Sintering --III. Rigid Inclusions" *Acta Metall.*, 36 (10) 2411-2416 (1988).
13. L. C. De Jonghe and M. N. Rahaman, "Sintering Stress of Homogeneous and Heterogeneous Powder Compacts", *Acta metall.*, 36 (1) 223-229 (1988).
14. M. N. Rahaman and L. C. De Jonghe, "Sintering of Particulate Composites Under a Uniaxial Stress", *J. Am. Ceram. Soc.*, 73 (3) 602-606 (1990).
15. M. N. Rahaman and L. C. De Jonghe, "Sintering of Ceramic Particulate Composites: Effect of Matrix Density", *J. Am. Ceram. Soc.*, 74 (2) 433-536 (1991).
16. L. C. De Jonghe and M. N. Rahaman, "A Loading Dilatometer", *Rev. Sci. Instrum.*, 55 (12) 2007-2010 (1984).
17. M. N. Rahaman, L. C. De Jonghe, and R. J. Brook, "Effect of Shear Stress on Sintering", *J. Am. Ceram. Soc.*, 69 (1) 53-58 (1986).
18. G. W. Scherer and A. Jagota, "Effect of Inclusions on Viscous Sintering", *Ceramic Transactions*, in Press.

19. R. M. Christensen, Theory of Viscoelasticity pp. 16-20, 2nd Edition, Academic, New York (1982)
20. A. G. Evans, "Considerations of Inhomogeneity Effect in Sintering", J. Am Ceram. Soc., 65 (10) 497-501 (1982)
21. F. F. Lange and M. Metcalf, "Processing-Related Fracture Origins: II, Agglomerate Motion and Cracklike Internal Surfaces Caused by Differential Sintering", J. Am. Ceram. Soc., 66 (6) 398-406 (1983).
22. R. K. Bardia and G. W. Scherer, "On constrained Sintering-I. Constitutive Model For A Sintering Body", Acta Metall., 36 (10) 2393-2397 (1988).
23. R. K. Bordia and G. W. Scherer, "On Constrained Sintering-II. Comparison of Constitutive Models", Acta metall., 36 (10) 2399-2409 (1988).
24. S. Andareson and I.A. Aksay, "Sintering with Rigid Inclusions: Pair Interactions", J. Am. Ceram. Soc., 73 (1) 54-60 (1990).
25. G. W. Scherer and A. Jagota, "2-Dimemsional Simulation of Sintering with Rigid Inclusion", in press.
26. Y. Yamada and K. Iwata, "Finite Element Analysis of Thermal-Viscoelastic Material", Research of Productions, 24 165-170 (1972).
27. O. C. Zienkiewicz, Finite Element Method , pp. 451-457, McGraw-Hill, New York,(1979).
28. A Jagota and P. R. Dawson, "Simulation of The Viscous Sintering of Two Particles", J. Am. Ceram. Soc., 73 (1) 173-177 (1990)

29. D. R. J.Owen and E. Hinton, Finite Element in Plasticity , pp. 275-279, Pineridge Press Limited, Swansea U.K.,(1980)
30. G. Berg and P. Grau, "Estimating the Viscosity of Viscoelastic Solid Based on a three parameter Model", J. Am. Ceram. Soc., 72 (11) 2187-2188 (1989)
31. R. M. Christensen, Mechanics of Composite Materials , pp. 31-70 John Wiley and Sons, New York, (1979)
32. W. N. Findley, J S. Lai and K. Onaran, Creep and Relaxation of Nonlinear Viscoelastic Materials , pp. 64-68, North-Holland Publishing Co. (1976)

### **3. PUBLICATIONS**

1. M. N. Rahaman and L. C. de Jonghe, "Sintering of Ceramic Particulate Composites: Effect of Matrix Density", *J. Am. Ceram. Soc.*, 74 [2] 433-436 (1991).
2. D-Y. Jeng and M. N. Rahaman, "Sintering of Amorphous Mullite with Crystalline Inclusions", *Ceram. Eng. Sci. Proc.*, in press.
3. M. N. Rahaman and C-L. Fan, "Sintering of Model Ceramic Particulate Composites, I: Conventionally Processed Composites", *J. Am. Ceram. Soc.*, in preparation.
4. C-L. Fan and M. N. Rahaman, "Sintering of Model Ceramic Particulate Composites, II: Slip Cast Composites", *J. Am. Ceram. Soc.*, in preparation.
5. C-L. Hu and M. N. Rahaman, "Sintering of Model Ceramic Particulate Composites, III: Coated Particles", *J. Am. Ceram. Soc.*, in preparation.
6. R. E. Dutton and M. N. Rahaman, "Effect of Inclusions on the Viscosity of Glass", *J. Mater. Res.*, in preparation.
7. H. Wei and L. R. Dharani, "Effect of Microcracking on the Densification Rate of a Ceramic Matrix Composite", Internat. Conf. on Composite Materials, July 15-19, 1991. Honolulu, Hawaii.
8. H. Wei and L. R. Dharani, "Analysis of Sintering Cracks in a Ceramic with a Rigid Inclusion", 21st Midwestern Mechanics Conference, August 13-16, 1991. Houghton, MI.

#### **4. PROFESSIONAL PERSONNEL**

##### Investigators:

M. N. Rahaman, Principal Investigator.  
L. R. Dharani, Co-principal Investigator.  
R. E. Moore, Senior Investigator.

##### Graduate Students:

R. E. Dutton, Ph.D. candidate.  
C-L. Hu, Ph.D. candidate.  
H. Wei, Ph.D. candidate.  
C-L. Fan, M.S. candidate.

#### **5. INTERACTIONS**

##### 5.1. Presentations

M. N. Rahaman and D-Y. Jeng, "Sintering of Amorphous Mullite with Crystalline Inclusions", Am. Ceram. Soc. Engineering Division Meeting, January 13-16, 1991, Cocoa Beach, FL.

M. N. Rahaman, "Constrained Sintering of Ceramic Composites and Thin Films", Invited Seminar, February 21, 1991, University of Washington, Seattle.

## 5.2. Consultative Function

Consultative visit by M. N. Rahaman, Principal Investigator, to the University of California, Berkeley, Lawrence Berkeley Laboratory, Center for Advanced Materials, Structural Ceramics Program, to review areas of mutual interest in "Sintering of Ceramics and Composites". February 20, 1991. Professor L. C. De Jonghe, Professor of Ceramics and Staff Senior Scientist.

## APPENDIX

### AN ANALYTICAL VISCOELASTIC SOLUTION OF 3-REGION COMPOSITE SPHERE MODEL

For the 2-region composite sphere in which the core is rigid, the elastic solution is as follows: In the spherical coordinate( $r, \theta, \phi$ ), the displacements is given by

$$u_r = u(r)$$

$$u_\theta = u_\phi = 0$$

Equation of equilibrium in terms of displacements is

$$\frac{\partial^2 u}{\partial r^2} + \frac{2}{r} \frac{\partial u}{\partial r} - \frac{2u}{r^2} = 0$$

for which the solution is given by

$$u = Cr + \frac{D}{r^2}$$

Using the kinematic relations

$$\varepsilon_r = \frac{\partial u}{\partial r}$$

$$\varepsilon_\theta = \varepsilon_\phi = \frac{u}{r}$$

the stresses can be written as

$$\sigma_r = 2\mu \left[ \frac{\partial u}{\partial r} + \frac{v}{1-2v} e \right] - 3K\varepsilon_f$$

$$\sigma_\theta = \sigma_\phi = 2\mu \left[ \frac{u}{r} + \frac{v}{1-2v} e \right] - 3K\varepsilon_f$$

$$\text{where } e = \frac{\partial u}{\partial r} + 2 \frac{u}{r}, \text{ and } K = \frac{E}{3(1-2v)}$$

The appropriate boundary conditions are

$$u(a) = 0, \quad \sigma(b) = P_b$$

where  $P_b = 0$  if no external traction is applied. The constants C and D can be determined

$$C = -\frac{D}{a^3} = \left( \frac{P_b}{3K} + \varepsilon_f \right) \frac{1+v}{1+v+2v_i(1-2v)}$$

where  $v_i = (\frac{a}{b})^3$  is the volume fraction of the core. So that

$$u_r(r) = \frac{1+v}{1+v+2v_i(1-2v)} \left( \frac{P_b}{3K} + \varepsilon_f \right) \left( r - \frac{a^3}{r^2} \right)$$

$$\sigma_r(r) = \frac{1}{1+v+2v_i(1-2v)} \left\{ [1+v+2(1-2v) \frac{a^3}{r^3}] P_b + 4(1+v)\mu\varepsilon_f \left( \frac{a^3}{r^3} - v_i \right) \right\}$$

$$\sigma_\theta(r) = \sigma_\phi(r) = \frac{1}{1+v+2v_i(1-2v)} \left\{ [1+v-2(1-2v) \frac{a^3}{r^3}] P_b - 4(1+v)\mu\varepsilon_f \left( \frac{a^3}{2r^3} + v_i \right) \right\}$$

The mean stress is

$$\sigma = \frac{1}{3} (\sigma_r + \sigma_\theta + \sigma_\phi) = \frac{2}{3} \mu \left( e + \frac{3v}{1-2v} e \right) - 3K\varepsilon_f = K(e - 3\varepsilon_f)$$

$$= \frac{1}{1 + v + 2v_i(1 - 2v)} \{(1 + v)P_b - 4v_i(1 + v)\mu\varepsilon_f\}$$

so that

$$e = \frac{1 + v}{1 + v + 2v_i(1 - 2v)} \left( \frac{P_b}{K} + 3\varepsilon_f \right)$$

By the correspondence principle, the viscoelastic solution can be obtained.

Denoting

$$\bar{f}(s) = L\{f(t)\} = \int_0^\infty f(t)e^{-st}dt$$

The Laplace transform of equilibrium equation is

$$\frac{\partial^2 \bar{u}}{\partial r^2} + \frac{2}{r} \frac{\partial \bar{u}}{\partial r} - \frac{2\bar{u}}{r^2} = 0$$

The general solution form of the above equation is

$$\bar{u} = \bar{C}r + \frac{\bar{D}}{r^2}$$

Assuming  $v(t) = \text{constant}$ , then the Laplace transform of displacement and stresses are

$$\bar{u}_r(r) = \frac{1 + v}{1 + v + 2v_i(1 - 2v)} \left( \frac{\bar{P}_b(s)}{3s\bar{K}(s)} + \bar{\varepsilon}_f(r - \frac{a^3}{r^2}) \right)$$

$$\bar{\sigma}_r(r) = \frac{1}{1+v+2v_i(1-2v)} \left\{ [1+v+2(1-2v) \frac{a^3}{r^3}] \bar{P}_b(s) + 4(1+v)s\bar{\mu}(s)\bar{\varepsilon}_f(\frac{a^3}{r^3} - v_i) \right\}$$

$$\bar{\sigma}_\theta(r) = \bar{\sigma}_\phi(r) = \frac{1}{1+v+2v_i(1-2v)} \left\{ [1+v-2(1-2v) \frac{a^3}{r^3}] \bar{P}_b(s) - 4(1+v)s\bar{\mu}(s)\bar{\varepsilon}_f(\frac{a^3}{2r^3} + v_i) \right\}$$

The Laplace transform of mean stress:

$$\bar{\sigma} = \frac{1}{1+v+2v_i(1-2v)} \left\{ (1+v)\bar{P}_b(s) - 4v_i(1+v)s\bar{\mu}(s)\bar{\varepsilon}_f \right\}$$

The Laplace transform of volumetric strain:

$$\bar{\varepsilon} = \frac{1+v}{1+v+2v_i(1-2v)} \left( \frac{\bar{P}_b(s)}{s\bar{K}(s)} + 3\bar{\varepsilon}_f \right)$$

For  $P_b(t) = 0$ ,

$$e = \frac{3(1+v)}{1+v+2v_i(1-2v)} L^{-1}\{\bar{\varepsilon}_f\}$$

$$= \frac{3(1+v)}{1+v+2v_i(1-2v)} \varepsilon_f$$

$$\sigma = - \frac{4(1+v)v_i}{1+v+2v_i(1-2v)} L^{-1}\{s\bar{\mu}(s)\bar{\varepsilon}_f\}$$

The result shows that no matter what viscoelastic constitutive models are used, there is no difference in volumetric strain between the elastic and viscoelastic cases for the composite sphere model under the condition of no external traction and constant poisson's ratio. However, the region outside the composite sphere consists of a viscoelastic matrix and dispersed rigid inclusions at the same volume fraction as the core. The outside region

can be treated as a homogeneous medium with different constitutive parameters and shrinking rate from the intermediate region. Therefore it is reasonable to assume  $P_b \neq 0$ . There are two ways to determine  $P_b$ , one of them is to use the so called self-consistent model, the other is a three region composite sphere model. It is necessary to know the constitutive parameter and free strain rate for the outside region.

Eshelby formula and Hashin-Shtrikman equations for shear and bulk moduli of a composite containing dispersed inclusions [31] are

$$\mu_c = \mu + \frac{5v_i\mu(3K + 4\mu)}{6(1 - v_i)(K + 2\mu)}$$

$$K_c = K + v_i(K - \frac{4}{3}\mu)$$

Using the three region composite sphere model, we can get the  $P_b$  for the elastic case, that is

$$P_b = 4\mu_c \left[ \frac{\left(\varepsilon_f - \varepsilon_{fc} - v_i\left(\varepsilon_f + \frac{4\mu}{3K}\varepsilon_{fc}\right)\right)}{1 + \frac{4\mu}{3K}v_i + \frac{4\mu_c}{3K}(1 - v_i)} \right]$$

$$\varepsilon_{fc} = -(1 - v_i)\left[\varepsilon_f + \frac{\sigma}{3K}\right]$$

$$\sigma = 3K \left[ \frac{\left(\varepsilon_f + \frac{4\mu_c}{3K}\varepsilon_f\right)}{1 + \frac{4\mu}{3K}v_i + \frac{4\mu_c}{3K}(1 - v_i)} \right]$$

The corresponding viscoelastic solution for  $P_b(t) \neq 0$  may be solved by the correspondence principle and the Laplace transform once the shear and bulk relaxation functions or creep functions are known.

The relaxation and creep function may be so complicated, however, as to be nontransform type. There are also several other limitations in employing this solution in the analysis of sintering problems. For example, the poisson's ratio is not constant and the deformation is not infinitesimal through the sintering process. However the nature of the solution gives out some insight into the problem. For example, the viscoelastic volumetric strain is the same as the elastic volumetric strain if the poisson's ratio is assumed to constant , even if the external traction  $P_s(t) \neq 0$ .